UNIVERSITAT POLITÈCNICA DE CATALUNYA
BARCELONATECH
Escola d'Enginyeria de Barcelona Est

UNDERGRADUATE THESIS PROJECT

Materials Engineering Degree

MICROMECHANICS IN ADDITIVELY MANUFACTURED METALS USING ELECTRON BEAM-BASED POWDER BED FUSION

Memory and Annexes

Author: Francesc Barberá Flichi
Director: Emilio Jimenez Piqué
Co-directors: Laia Ortiz Membrado, Carlos Botero

Convocation: June 2023

Resum

Els metalls obtinguts mitjançant fusió de llits de pols (PBF, *Powder Bed Fusion*), concretament per la tècnica de fusió per feix d'electrons (EB, *Electron Beam*), poden tenir propietats diferents, ja siguin físiques o mecàniques, depenent de la deposició d'energia del feix d'electrons i d'altres paràmetres de fabricació. El fet de conèixer les propietats mecàniques dels materials permet explicar el seu comportament davant d'estímuls externs, i una tècnica molt utilitzada per fer-ho és la de realitzar assajos de nanoindentació.

En el present estudi, s'han analitzat una sèrie de mostres de metalls produïts mitjançant PBF-EB utilitzant diferents paràmetres de manufactura mitjançant assaigs de nanoindentació amb l'objectiu de conèixer els canvis que es produeixen a les propietats mecàniques (concretament, la duresa i el mòdul elàstic), i correlacionar-los amb la microestructura.

Paral·lelament, s'han dut a terme anàlisis estadístics de les dades obtingudes als assajos mitjançant algoritmes d'aprenentatge automàtic (*Machine Learning*). Concretament, s'han aplicat mètodes d'agrupació (*clustering*), amb la intenció de crear un mètode robust que sigui capaç de, a partir de les dades dels assaigs de nanoindentació, identificar determinades característiques del material, concretament quines fases conté, com estan distribuïdes i les orientacions cristal·lines que tenen.

Resumen

Los metales obtenidos mediante fusión de lechos de polvo (PBF, *Powder Bed Fusion),* concretamente por la técnica de fusión por haz de electrones (EB, *Electron Beam*), pueden tener propiedades diferentes, ya sean físicas o mecánicas, dependiendo de la deposición de energía del haz de electrones y otros parámetros de fabricación. El hecho de conocer las propiedades mecánicas de los materiales permite explicar su comportamiento frente a estímulos externos, y una técnica muy utilizada para ello es la de realizar ensayos de nanoindentación.

En el presente estudio, se han analizado una serie de muestras de metales producidos mediante PBF-EB usando diferentes parámetros de manufactura mediante ensayos de nanoindentación con el objetivo de conocer los cambios que se producen en las propiedades mecánicas (concretamente, la dureza y el módulo elástico), y correlacionarlos con la microestructura.

Paralelamente, se han llevado a cabo análisis estadísticos de los datos obtenidos en los ensayos mediante algoritmos de aprendizaje automático (*Machine Learning*). Concretamente, se han aplicado métodos de agrupación (*clustering*), con la intención de crear un método robusto que sea capaz de, a partir de los datos de los ensayos de nanoindentación, identificar determinadas características del material, concretamente qué fases contiene, cómo están distribuidas y sus orientaciones cristalinas.

Abstract

Metals obtained by Powder Bed Fusion (PBF), specifically by Electron Beam (EB), can have different properties, either physical or mechanical, depending on the electron beam energy deposition and other manufacturing parameters. The knowledge on the mechanical properties of materials makes it possible to explain their behavior in the face of external stimuli, and a widely used technique for this is to perform nanoindentation tests.

In the present study, a set of metallic samples produced by PBF-EB using different manufacturing parameters have been analyzed performing nanoindentation tests with the aim of understanding the changes that occur in the mechanical properties (specifically, hardness and elastic modulus), and correlating them with the microstructure.

At the same time, statistical analysis of the data obtained in the tests was carried out by Machine Learning algorithms. Specifically, clustering algorithms have been applied, with the intention of creating a robust method capable of identifying, from the nanoindentation test data, identify certain characteristics of the material, specifically which phases it contains, how they are distributed and the crystalline orientations they have.

Agradecimientos

El desarrollo de este estudio no hubiera sido posible sin la ayuda de Laia Ortiz, Emilio Jimenez y Carlos Botero. Gracias a ellos, no sólo he podido llevar a cabo este proyecto, si no también crecer profesionalmente y adquirir conocimientos muy valiosos. De nuevo, gracias por esta oportunidad.

Este proyecto se lo dedico a mi familia y a mi pareja, que siempre han estado ahí cuando los he necesitado. Que estén orgullosos de mí es lo que más me importa.

"Si alguien ya lo ha hecho, tú también puedes. Si nadie lo ha hecho, tú puedes ser el primero"

Glossary

AM: Additive Manufacturing
SEM: Scanning Electron Microscopy
ISE: Indentation step Effect
EB: Electron Beam
PBF: Powder Bed Fusion
EBSD: Electron Backscatter Diffraction
V4E: Vanadis 4 Extra steel
BN: Boron carbides
SEM: Scanning Electron Microscope
GMM: Gaussian Mixture Model
HAC: Agglomerative Hierarchical Clustering
DBSCAN: Density-Based Spatial Clustering of Applications with Noise
EM: Expectation Maximization
GMM: Gaussian Mixture Model
EDS: Energy-Dispersive X-ray Spectroscopy
BN: boron carbides

Index

1. Introduction

Micromechanics, also referred to as continuum micromechanics of materials, study the connections between microstructure and properties of multi-phase materials. There are two principal objectives that micromechanics intends to fulfill: the first one is homogenization; the process by which macroscopic behavior is inferred from the geometrical arrangement and material responses of the elements. The second one is localization; describing the microscopic fields that correlate to specific macroscale fields [1]. Some of the most common micromechanics methods are those computational based, such as serial sectioning, statistical synthetic or multi-cell, which provide better estimations of properties than analytical methods [2].

Nanoindentation correlates with micromechanics by the fact that it can be used in the micromechanical models mentioned before and with finite element analysis (FEA), to predict the intrinsic mechanical properties by measuring it in individual phases in heterogeneous materials [3].

As nanoindentation provides a high-throughput data due to the high-speed feature, the use of statistical methods allows the intrinsic mechanical properties determination of the constitutive phases of the material [4]. Because of this, unsupervised machine learning techniques are applied, also called cluster analysis, that consists in the partitioning of data into relevant subgroups when the number of subgroups is unknown [5]. Some of these techniques include Gaussian Mixture Model (GMM), K-means clustering, and Hierarchical Agglomerative clustering (HAC), among others.

Additive Manufacturing (AM) is a manufacturing technique, also known as 3D printing, which is based on layer-by-layer material deposition principle. A key advantage of AM is the ability to manufacture complex-shape parts that are impossible to obtain through traditional techniques [6].

One of the most important AM technologies for metals is the PBF-EB (Electron Beam based Powder Bed Fusion) due to its ability to achieve advanced control over the manufacturing process. PBF-EB technologies have been used to manufacture different types of metallic alloys including single phase stainless steels such as 316L [7]–[9] and more complex multiphase materials such as super duplex [10] or cold-work tool steels such as V4E, in which carbides are formed during manufacturing [11], [12]. Moreover, another advantage of this technique is that it allows for local tailoring of the material microstructure, so that different material properties in a single material is possible, such as mechanical, thermal, and electrical properties [13]–[15]. Furthermore, it is also possible to use different powders and combine them during manufacturing in multiple separate stages, resulting in a multi-material component whereby the components are built with different alloys containing different phases [16].

By combining high-speed nanoindentation with clustering techniques, a comprehensive understanding of the mechanical properties of the AM materials can be achieved. This analysis can facilitate the

identification of different mechanical properties associated with both phases and even crystal orientations.

It is known that differences in microstructure and phases imply different properties [17]–[20]. Therefore, obtaining information about the phase's quantity and distribution through the material is desired, as it would allow us to understand the overall material behavior, and the only way to reach this is to perform nanoindentation tests.

Nanoindentation tests, are widely used for measuring the mechanical properties of thin films and small volumes of material, enabling the accurately measurement of nano-Newton forces [21]. As it is possible to make indentations with a high-speed rate of 1 indentation per second, high speed indentation maps with the material properties (and thus phases distribution) are obtained [3].

At this point, it is possible to correlate the property maps with the microstructure of the material. However, this correlation is visually apparent, but not quantitative. To quantify the phases information, the data must be deconvoluted using statistical methods [22].

It must be highlighted that both nanoindentation and statistical analysis are very useful and well suited for PBF-EB manufactured materials, since they present local changes in composition and microstructure, which consequently result in local changes in mechanical properties. In this study, a group of metallic samples manufactured using PBF-EB are analyzed by nanoindentation tests and the data is treated using Gaussian Mixture Model (GMM) algorithm.

1.2. Motivation

Multiple articles have studied the correlation between the property's maps derived from nanoindentation tests and analyzed it using statistical methods based on clustering algorithms assuming that the distribution follows a Gaussian [4], [23]–[26]. Also, the maps included on these studies concentrates on localized regions –because it is sufficient to measure nano-scale properties – but it is no common to see nanoindentation maps with relatively large dimensions with also high resolution, due to the time needed to perform it.

It has been thought that performing high dimension nanoindentation properties maps would be of great interest, since it would enable the possibility to apply different statistical methods, compare it and discuss which one works better.

Another point to consider is that data deconvolution is done considering that mechanical properties can be approximated by a Gaussian function [4], [24], [26]–[28]. However, in some cases this model doesn't fit the data properly, as is shown in Figure 1, where it can be seen a superposition of the green

and red phases, and experimental data unfitted. Therefore, finding a model able to fit all the data obtained through the nanoindentation tests is of great interest.

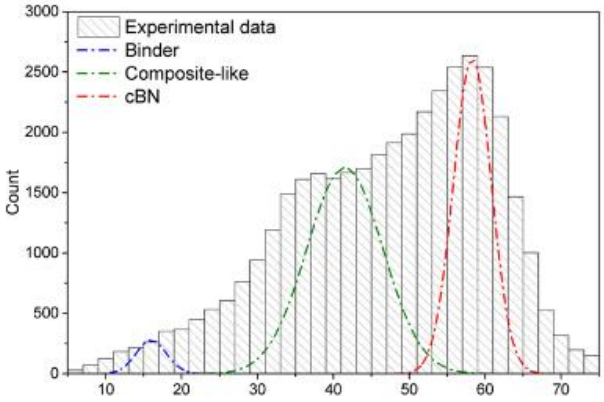

Figure 1: example of a Gaussian model fitting. Source: [4].

In this context, high dimensions nanoindentation tests are conducted in this study to analyze big areas of the samples and obtain property maps, with the objective to correlate it with the maps obtained doing cluster analysis and to verify the accuracy level of the statistical method. Additionally, characterization techniques such as Electron Backscattered Diffraction (EBSD) and Scanning Electron Microscopy (SEM) were also applied to correlate the sample microstructure and grain orientation with the overall mechanical results.

1.3. Objectives

In this project, the following objectives are to be achieved:

- Understand the basic theory on nanoindentation, as well as the use of the equipment, and its limitations.
- Successfully perform nanoindentation tests to a group of additively manufactured samples, plot the hardness and modulus maps, and analyze the obtained results.
- Search and apply different statistical methods to deconvolute the data obtained through the tests and choose the one able to fit the largest amount of data.
- Correlate the hardness and modulus maps with the microstructure observed through different analysis techniques such as Electron Backscattered Diffraction (EBSD) and Energy Dispersive Spectroscopy (EDX).

1.4. Scope of the work

This work aims to reach all the objectives proposed in the 2.1 section, since there are no restrictions other than the available time to perform all the tests and considering that the iMicro nanoindenter and other machines such as the Vibromet or SEM are very requested.

Sample preparation must be considered too, as it takes a considerable amount of time. To perform nanoindentation tests, a high level of sample preparation is not strictly required, but it is necessary for EBSD analysis. This process has no associated difficulty but must be performed accurately because a small error could imply repeating some steps of the sample preparation, as it had been the case.

Another aspect to consider is that the iMicro presented several technical problems that has limited even more the available time, such as tip calibration failures, actuator failures or errors during the data acquisition, among others.

1.5. State of the art

1.5.1. High-speed nanoindentation

The concept of high-speed nanoindentation refers to the use of the classical nanoindentation technique at high speeds. Recently, advances on this field have been reached such as the discovery of alternative materials for indenters [29], new indentation systems able to indent at high temperatures with low thermal drift [29], the development of a laser heating technique to measure high-temperature indentations [30], and improvements on the testing speed rates, which has meant that the nanoindentation technique is now classified as a high-throughput mechanical test [31]. In fact, high-speed nanoindentation is known as high-throughput nanoindentation too. On this study, focus has been put on the high-throughput nanoindentation technique, since analyze statistical methods is desired.

The most recent advances consist of the improvement of the testing speed rates, which means that the testing processes have been accelerated until reaching a 6 indents per second speed. This allows the development of studies that require a large number of tests in a reasonable amount of time. For example, a 10.000 nanoindentations map can be done in less than an hour [31].

1.5.2. High-speed nanoindentation statistical analysis

As it has been mentioned before, high-speed nanoindentation has opened the door to perform mechanical property maps containing a considerable number of indentations in a reasonable amount

of time, thanks to the test speed rate of 6 indents per second. This implies that datasets with enough density to perform statistical analysis will be obtained. Moreover, combining these maps with other techniques that allow the information acquirement about microstructure, crystallography, or chemical composition makes possible to take a more in-depth understanding point of view. This has been recently applied in for instance titanium [32], aged Inconel [33], meteorites [34] and Al-Cu alloys [35].

The most common methodology used for statistical analysis of the nanoindentation tests data is the use of a simple Gaussian fit [36]. Nevertheless, this method involves several problems, beginning with the assumption that the mechanical properties follow a Gaussian distribution, which is not always true. Also, choosing the optimal indentation imprint size is essential to be sure that individual phases are captured. Moreover, the fact that this method requires an initial estimation of the number of distributions to be fitted – which is done manually based on previous knowledge of the case study – is the most important drawback due to the incorrect phase identification and/or the incorrect properties attribution. For this reason, is important to establish a method that reduces or eliminates, as far as possible, the disadvantages described before. Recent studies applied another clustering algorithms such as K-means and 2D Gaussian [22], [37], [38], and semi-supervised machine learning algorithms [39]–[41].

The Gaussian mixture model (GMM) has been applied to multiple recent studies involving nanoindentation studies and could be the best method to perform the phase identification of nanoindentation tests data [42]–[45]. The main advantage of the GMM is that less assumptions are needed to perform a good phase identification and seems to work better.

1.5.3. Nanoindentation on additively manufactured metals

Nanoindentation tests are being applied to additively manufactured metals with multiple purposes. Some of them are evaluating its mechanical properties depending on different manufacturing parameters, analyze the microstructure and evaluating the corrosion resistance, among others [46]–[49]. The main objective of these studies is to enlarge the possibilities that additively manufactured metals could offer by improving its mechanical properties.

2. Theorical aspects

2.1. Nanoindentation

Nanoindentation is a localized mechanical testing technique similar to a hardness test but differs from the fact that the load and displacement into the surface of the indenter measurements are continuously measured. While an indenter of known geometry and material is pressed against the sample surface, load as a function of displacement is registered, resulting in data from where the hardness and elastic modulus is determined. Its widely used to evaluate mechanical properties of heterogeneous microstructures on the nanometric scale.

This technique presents several benefits, such as the hardness and elastic modulus obtaining without imaging the resulting indentations, the minimal sample preparation requirement, the non-destructive feature, and the availability to apply it to small volumes of material, in the order of about 1 mm^3.

Nevertheless, there are a few drawbacks that must be considered. For example, surface roughness becomes critical and could affect to the measured properties if the indenter don't penetrate deeply enough, and finding an appropriate testing region could be a time-consuming task [25], [50].

2.1.1. Oliver and Pharr method

The most widely method used for the hardness and elastic modulus calculus is the Oliver and Pharr method, which enables the measurement of the above-mentioned properties with a single test using a Berkovich indenter.

After the test, a load-displacement curve (P-h curve) is obtained and represents all the collected data. Notice that it is necessary to record all the data, from the beginning to the end of the test, to get the loading and unloading curves. Once those curves are obtained, the unloading one is fitted with a power-law relation *(Ec.1.)* to calculate the elastic unloading stiffness *(Ec.2.)*:

$$P = \alpha\left(h - h_f\right)^m \qquad \text{(Ec.1.)}$$

$$S = \frac{dP}{dh}\Big| h_{max} \qquad \text{(Ec.2.)}$$

Where α and m are fitting parameters, h_f the final depth and S the elastic unloading stiffness.

The contact depth (h_c) is calculated with the following expression:

$$h_c = h_{max} - \varepsilon \frac{P_{max}}{S} \qquad \text{(Ec.3.)}$$

Where P_{max} corresponds to the peak indentation load and $\mathcal{E}$ is a constant which value depends on the indenter geometry (Ɛ ≈ 0.75 for Berkovich indenter).

Knowing the contact depth, the contact area ($A(h_c)$) must be calculated. This is done by using the shape function at the contact depth (see Ec.4.) of the indenter, which describes the cross-sectional area of the indenter to the distance from its tip.

$$A = f(h_c) = A(h_c) \qquad \text{(Ec.4.)}$$

It's very important to note that tips are not perfect, and the relationship between the area and the contact depth must be recalculated by calibrating the indenter tip using a material with well-known properties, such as fused silica or aluminum.

Once the projected contact area is calculated, hardness and effective elastic modulus are obtained from the following expressions:

$$H = \frac{P_{max}}{A} \qquad \text{(Ec.5.)}$$

$$E_{eff} = \frac{1}{\beta}\frac{\sqrt{\pi}}{2}\frac{S}{\sqrt{A}} \qquad \text{(Ec.6.)}$$

Where β is a constant that depends on the indenter geometry (β = 1.034 for Berkovich indenter).

The effective modulus consider that elastic deformation occurs in both the sample and the indenter, and its definition is detailed in Ec.7.:

$$\frac{1}{E_{eff}} = \frac{1-\nu^2}{E} + \frac{1-\nu_i^2}{E_i} \qquad \text{(Ec.7.)}$$

Being E and ν the elastic modulus and Poisson's ratio for the sample, and E_i and ν_i the same parameters for the indenter [50].

2.1.2. Indentation Spacing

The concept of indentation spacing refers to the space between indents and it's one of the most important parameters when carrying out nanoindentation tests, especially when the volume we want to measure its properties is small, where measuring local variations in mechanical properties is priority.

A recent study made by P. Sudharshan Phani and W. C. Oliver revealed that the minimum indent spacing should be 10 times the indentation depth, as it is demonstrated that this value is enough to

obtain acceptable results for a Berkovich tip [3]. When the indentation spacing is not enough, there is a high probability that results are affected by the overlapping of plastic deformation between indentations [51].

This parameter lets us know the maximum number of indentations a specific area can contain to be sure the results would be truthful. Therefore, tests performed following it will have the maximum possible resolution.

2.1.3. Indentation Size Effect

Indentation Size Effect is a small-scale phenomenon that consists of the increment on the yield strength that occurs, mostly, on micron or submicron sized samples. This yield strength growth is due to the sample dimensions approaching the average dislocation spacing and the presence of a limited number of defects on the material, controlled by plastic deformation.

It is assumed that plasticity can be described by classical continuum concepts, in which there is no inherent material length scale. As geometrically self-similar indenters (such as pyramidal and conical) have neither length scale, the hardness should be independent of the penetration depth. Nevertheless, numerous experimental procedures [52]–[55] have been made demonstrating that, effectively, hardness is dependent on the penetration depth

Two types of ISE have been found: the normal ISE, which consists of the yield strength – and therefore the hardness – increment at small depths, and the reverse ISE, which stands out for the decrement of the hardness at small depths (see Figure 2) [53].

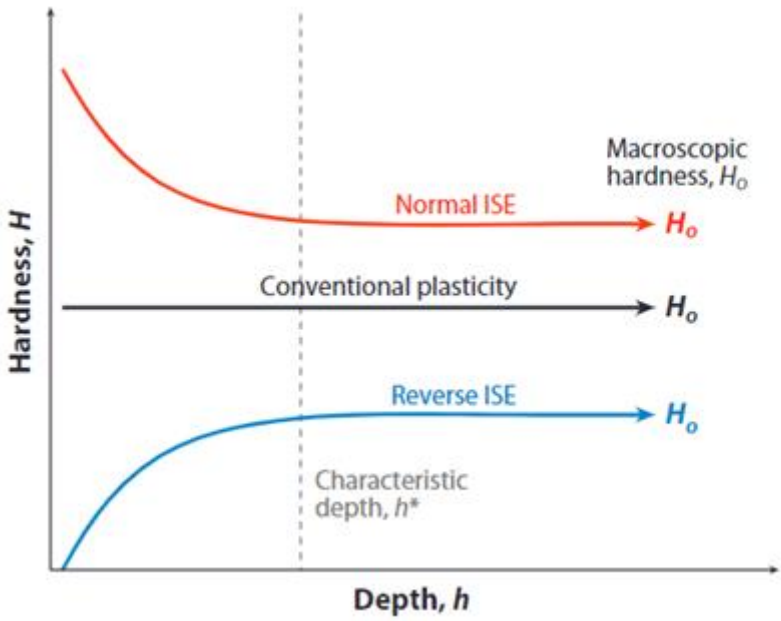

Figure 2: The two types of ISE, compared with the conventional plasticity. Source: [53].

It should be noted that is possible to know the minimum penetration depth from the ratio between the applied load and the stiffness squared as a function of penetration depth where mechanical properties would not change significantly [56]. It is interesting to keep this in mind to avoid undesired effects such as the mentioned ISE and the measures deviation induced by the roughness of the surface.

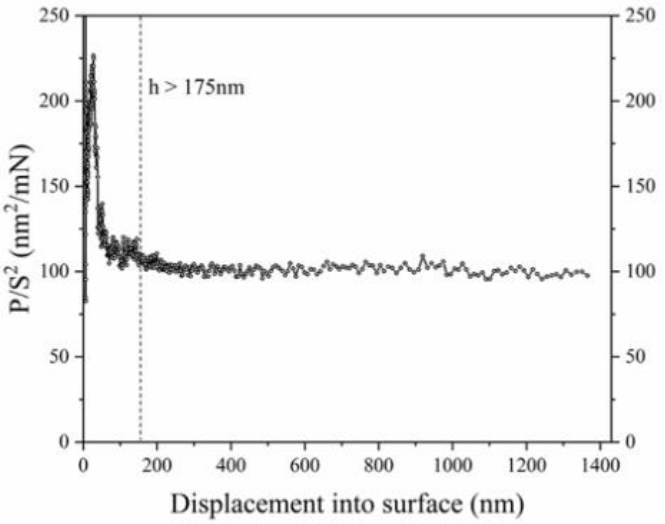

Figure 3: example of the obtaining of the minimum penetration depth. Ratio between the applied load and the stiffness squared (P/S^2) as a function of penetration depth (h) is represented. Source: [56].

2.1.4. Pile-up or sink-in

The Oliver and Pharr method does not account for possible errors induced by the presence of pile-up or sink-in phenomena. When pile-up occurs, the contact area is greater than the one calculated by the method (using Ec.4.), resulting in an overestimation of the measurements. This is caused by the fact that the method uses an elastic contact analysis to calculate the contact depth.

The ratio between the final indentation depth *(h_f)* and the depth of the indentation at peak load *(h_{max})* allow us to avoid these undesirable effects. h_f/h_{max} can only take values between 0 to 1, and when this ratio is close to 1, pile-up is considerable. It is also known that the degree of work hardening has an important role, increasing the pile-up when is low. However, when the ratio value is less than 0.7, pile-up can be considered negligible [21].

2.2. Statistical methodologies

As the nanoindentation tests are considered as a high-throughput mechanical tests, the use of statistical methodologies – which includes machine learning algorithms - are required to draw conclusions. There are different machine learning algorithms, for example regression, classification, clustering, and deep learning [57], but the most used to analyze the nanoindentation tests data are the clustering ones, as they can classify data in function of their mechanical properties, and therefore identifying the different phases of the material and crystallographic orientations.

2.2.1. Clustering algorithms

This type of algorithms is used in unsupervised machine learning - which the highlighted feature is that these are trained using unlabeled datasets and are allowed to act on that data without any supervision [58], [59] - to group data points based on their similarities. The groups in which the data points belong are known as clusters. On the nanoindentation field, the clusters represent the phases contained on the studied material.

Applying clustering algorithms to the data from the nanoindentation tests allow us to complement the mechanical property maps with quantitative information, as the maps only offers a qualitative approach.

The most common clustering methods - the Gaussian Mixture Model, K-means, hierarchical agglomerative (HAC), Density-Based Spatial Clustering of Applications with Noise (DBSCAN) will be described in the following chapters.

2.2.1.1. Expectation-Maximization (EM) clustering using Gaussian Mixture Model (GMM)

The standard phase identification method used in the nanoindentation field is the Gaussian Mixture Model (GMM) [28]. This model is a combination of multiples Gaussian distributions and is used to represent normally distributed subpopulations (the phases or crystallographic orientations) within an overall population (the whole dataset from the mechanical property maps).

When the data form a single peak, a Gaussian (or normal) distribution is used, which is defined by the following formula, known as the Probability Density Function:

$$y = \frac{1}{\sigma\sqrt{2\pi}} e^{\frac{-(x-\mu)}{2\sigma^2}} \qquad \text{(Ec.8.)}$$

Being μ the mean and σ the standard deviation.

For each point X its Y value is calculated. X represents the data, and Y the probability that the data are part of the curve. On the other hand, when there are multiple peaks (i.e., the data fit several Gaussian distributions), the Gaussian Mixture Model (GMM) is used, and the probability distribution function is:

$$N(\mu, \sum) = \frac{1}{(2\pi)^{\frac{d}{2}}\sqrt{|\sum|}} e^{-\frac{1}{2}(x-\mu)^T \frac{(x-\mu)}{\sum}} \qquad \text{(Ec.9.)}$$

Where $\sum$ is the covariance matrix of the Gaussian, *x* the number of datapoints and *d* the number of features in the dataset.

Ec.9. can also be expressed as:

$$p(x) = \sum_{j=1}^{K} w_j N(x|\mu_j, \sum_j) \qquad \text{(Ec.10.)}$$

$$\sum_{j=1}^{K} w_j = 1 \qquad \text{(Ec.11.)}$$

$$0 \leq w_j \leq 1 \qquad \text{(Ec.12.)}$$

Where w_j is the prior probability of the j^{th} Gaussian [60].

2.2.1.1. K-means clustering

The functioning of the algorithm consists in, first, selecting a random number of clusters and initializing its respective center points. The distance between each point and each group center is calculated to classify each point to the nearest group. The mean of all vectors in the group is calculated, and the group center is recalculated. Finally, this procedure is repeated until the algorithm converges, which succeed when the group centers don't change more than a specified value [61].

K-means present a few advantages compared to other models, such as the fact that the operation time is low – and therefore, treatment of large datasets is not a problem - and it is easy to understand how it works and how to implement it. However, there are some drawbacks that must be considered: this method is sensitive to outliers, it assumes that the density of the data is spherical and is sensitive to scale, which means that results may vary depending on the units of measurement used, among others [28]– [30].

2.2.1.2. Hierarchical Agglomerative Clustering (HAC)

The main objective of the HAC algorithm is to classify similar data in different clusters – as the other algorithms – but in a hierarchical way, representing the clusters in a hierarchical tree known as dendrogram. Its functioning is based on the following steps:

- Initializing: the algorithm starts with a set of N elements, being each one a single cluster.
- Distance matrix calculus: this matrix measures the similarity level between each couple of data points.
- Cluster union: based on the distance matrix calculus, the two clusters most similar to each other joint together.
- Distance matrix update: an update with the new similarity level of the new cluster with the other ones.
- Repeating the cluster union and the distance matrix update since the algorithm converge. This happens when there are no more clusters to joint or a special restriction is accomplished, for example having a certain number of clusters.
- Dendrogram representation of the clusters hierarchy.

The most highlighted advantages of this method are that specification of the number of clusters is no needed and that the dendrograms offer a more organized view of the clusters. Notwithstanding, it is not valid for large datasets due to the time complexity of the algorithm, being of $O(n^3)$. In addition, this method has a high sensitivity to noise and outliers [64], [65].

2.2.1.3. Density-Based Spatial Clustering of Applications with Noise (DBSCAN)

DBSCAN differs from the previous algorithms by the fact that is a density-based algorithm that its main function is to identify clusters with different shapes and sizes from a large amount of data, even if there are outliers and noise [66]. Its functioning is based on the following steps[67]:

- Definition of parameters: the neighborhood distance (eps) and the minimum number of data points to define a cluster (minPts).
- Core points selection and distance calculation: a data point from the dataset is selected and its distance from the other data points is determined. If the number of points inside the neighborhood distance equal or greater than the minimum number of data points to define a cluster, the selected point is considered as a core point.
- Cluster expansion: if the selected point is a core point, a new cluster is formed and the data points belonging to the neighborhood distance are classified to the cluster.
- Classification of the remaining data points: those that are not core points but belong to the neighborhood distance are considered as border points. The data points thar are not border or core points are considered as noise points.

It is a fast algorithm, therefore is valid to analyze large datasets and, as has been mentioned before, the presence of noise and outliers does not affect the appropriate function of it. But the most important feature is that DBSCAN can identify noise and outliers and exclude it from belonging to a cluster, which is not possible with another algorithms. This distinguishing is done by identifying data

groups that are separated of other ones by an empty space. However, there are several drawbacks that must be considered, such as the sensitivity to the choice of parameters and the need to have a clear separated points to do the clustering correctly [68], [69].

2.2.2. Clusters representation

Once the clustering algorithm is applied, a certain number of clusters are detected, and experimental data is fitted to a certain number of curves – also known as components -. There are three ways of representing them: superimposing the fitted curves of the phases on the experimental data histogram, plotting hardness vs modulus contour plots, or plotting X position vs Y position contour plots. These three representations complement each other.

2.2.2.1. Histograms

The main objective of this type of representation is to know how the statistical method has fitted the Gaussian distributions with the experimental data. On Figure 4, for example, is possible to clearly observe that the statistical method used identified three clusters, and seeing the histogram and distribution curves representation we can consider that all of them fits with the experimental data.

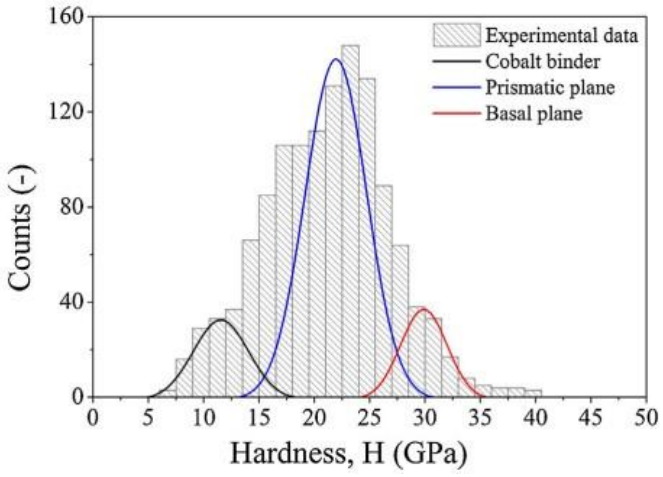

Figure 4: example of a histogram representation with three phases superimposed. Source: [24]

2.2.2.2. X position vs Y position contour plots

By applying this type of representation, it is possible to see the cluster identification that the clustering algorithm have done in a map-view style. This contour plots are usually compared with the nanoindentation maps to check the quality of the cluster identification.

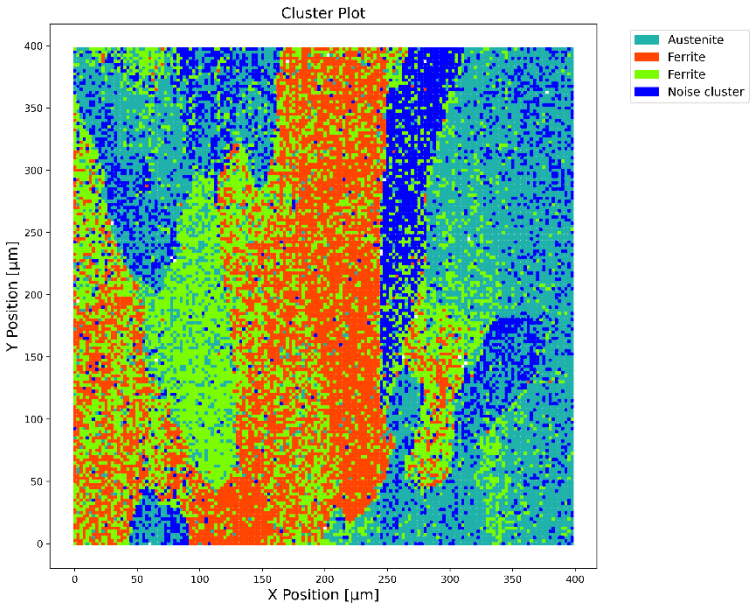

Figure 5: example of X position vs Y position contour plot of a 316L steel . Source: author image

2.2.2.3. Hardness vs modulus contour plots

This representation allows us to know which data points have been labeled to a specific cluster. Also, is a tool that allow us to identify which are the clusters that fits better to the experimental data. These will be the ones that have less dispersion on its data points, as it has been seen that the clusters with a high level of dispersion are, in fact, noise.

Figure 6 show an example of a hardness in function of modulus contour plot, and the light blue and orange clusters data points have less dispersion than those pertaining to the dark blue and green ones, indicating that the first two clusters have been done more accurately.

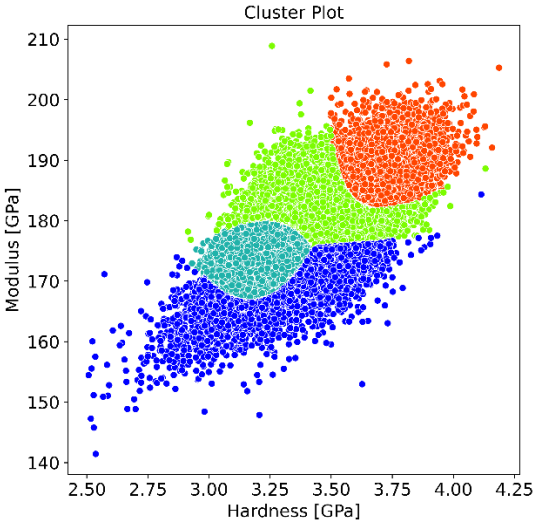

Figure 6: Example of hardness vs modulus contour plot for a 316L sample. Source: author image.

2.3. Characterization techniques

2.3.1. Electron Backscattered Diffraction (EBSD)

The hardware needed to perform the EBSD tests is composed by a crystalline sample tilted 70º, a phosphor screen, a sensitive camera, an insertion mechanism, electronics to control the SEM, a forescatter diodes and a computer running the specific software, as is shown in Figure 7:

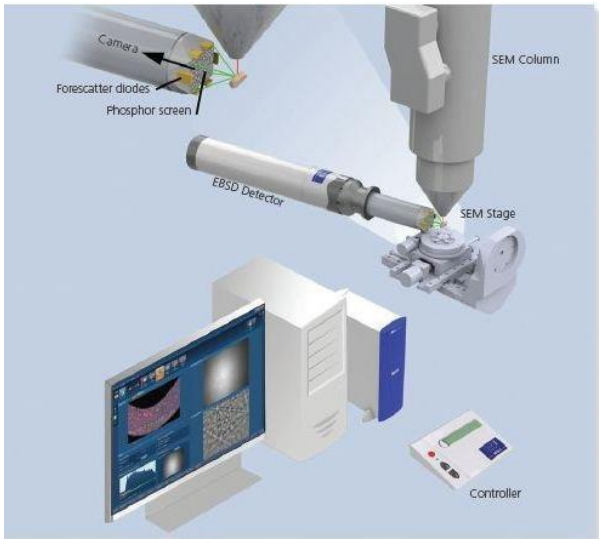

Figure 7: schematic representation of EBSD hardware. Source: [70].

When an electron beam is focused on the point of interest of the sample, the dispersion of the electrons of the material occurs thanks to its atoms. Some of them contact on atomic planes at determined angles that satisfy the Bragg equation:

$$n\lambda = 2dsin\theta \qquad \text{(Ec.13)}$$

Being λ the electron wavelength, θ the angle on incidence, *d* the spacing of the diffracting plane and *n* an integer.

When the electrons diffract, they create multiple paired cones that coincide with each diffraction plane, creating the called Kikuchi bands, that are visible on the phosphor screen. The Kikuchi bands are formed where the areas of enhanced electron intensity cross the screen [70]. Crystallographic orientation is obtained thanks to the fading or brightness of the diffraction spots coming from the crystals [71].

2.3.2. Scanning Electron Microscope (SEM)

The Scanning Electron Microscope (SEM) is a type of electron microscope used to obtain images of the samples by scanning the surface with a focused beam of electrons. Its function consists in the interaction between the atoms in the sample and the incident electrons, which produces various signals corresponding to useful information, such as the topography and the composition. Therefore, the microstructure of the sample material can be determined [72], [73].

Another similar characterization techniques can be performed using the SEM by attaching special detectors as, for example, the EDS – that will be explained below -.

2.3.2.1. Energy-Dispersive X-ray Spectroscopy (EDS)

The Energy-Dispersive X-ray Spectroscopy (EDS) is a surface analytical technique for identifying and quantifying elemental compositions in a small area of the studied material [74]. This technique separates the characteristic X-rays of each element present on the chemical composition into an energy spectrum and, using specific software, this spectrum is analyzed [75].

Although this technique is useful due to the high speed of data acquisition, the high efficiency of the detector, the ability to obtain important elemental information of the chemical composition and the fact that the analysis is non-destructive type [76], there are a few disadvantages that using this method involve, beginning with the impossibility of detecting small quantities of elements or those that have a low atomic number. Furthermore, low atomic number elements involve poor energy resolution of the obtained peaks [76]–[78].

3. Samples information

A total of 7 samples have been included in this project and are classified in 3 groups according to the strategies used for the manufacturing: “multilayered materials”, “microstructurally tailored materials”, and “multiphase and composite materials”.

An Arcam A2 machine was used to carry out the manufacturing process of the samples. Different configurations of the machine were used for obtaining the “multilayered”, “multiphase and composite materials” and for the “microstructurally tailored” ones. The samples classified as “microstructurally tailored” materials were manufactured using the standard configuration of the machine, which consists in fetching powder from both hoppers at the same time. On the other hand, for the manufacturing of the “multilayered” and some of the “multiphase and composite” samples, a reconfiguration of the hoppers consisting of filling the hopper with different metal powders according to the desired composition of the sample to be manufactured has been used [6]. This reconfiguration also allows the layer-by-layer manufacturing of multi-materials [16].

The composition of the feedstock materials is specified on Table 1:

Table 1: Composition of metal powders. Source: [10], [13], [16]

Element [wt%]	**Fe**	**Cr**	**Ni**	**Mo**	**Mn**	**Si**	**C**	**Ti**	**Al**	**V**	**N**
316L	Balance	16-18	12-14	2-3	1.4	0.7	0.03	-	-	-	-
V4E	Balance	4.7	-	3.4	0.4	0.4	1.4	-	-	3.7	-
SD 2507	Balance	25	7	4	<1.2	<0.8	<0.3	-	-	-	0.3

Information about the BN composition is specified on the next reference: [79].

More information about the samples is specified in the following chapters.

3.1. Multilayered materials

Multilayered materials were obtained by placing 2 different powders; 316L and V4E (see Table 1), in each of the hoppers of the PBF-EB machine, and by steering the powder fetched to the build plate in

an alternate way. Different configurations were obtained: a transition structure, and a gradient structure, as described in the following sections.

3.1.1. 316L + V4E with transition structure

This sample has been manufactured with a base of 45 layers of 316L steel, then 10 alternating layers with V4E and the rest of only V4E, as shown in Figure 8 a) [16].

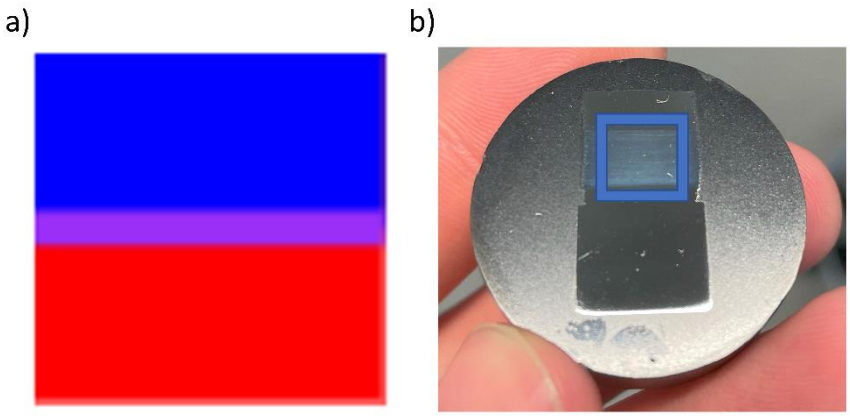

Figure 8: a) schematic representation of composition structure for the 316L steel with V4E. Source: [16]. *b) image of the 316L+V4E sample with transition structure. Source: author image*

The region where the nanoindentation tests were performed is marked with the blue square on Figure 8 b).

3.1.2. 316L + V4E with gradient structure

The same metal powders have been used to manufacture this sample, but its structure is different, being compounded by 28 layers of 316L as a base, then 72 layers alternating V4E with a gradient, as shown in the scheme on Figure 9 a) [16].

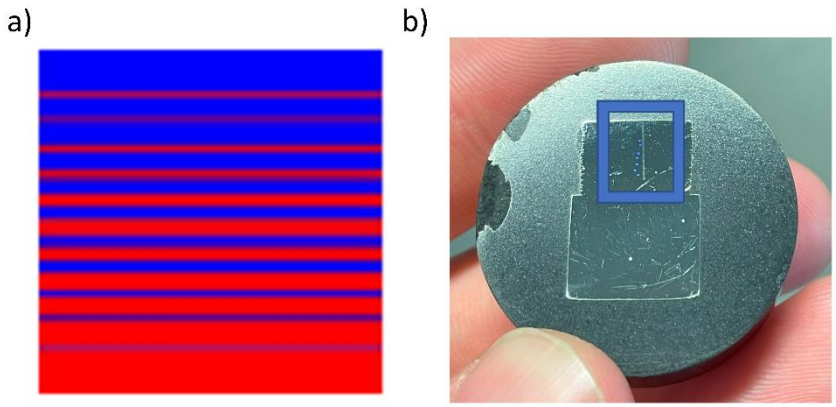

Figure 9: a) schematic representation of composition structure for the 316L steel with V4E. Source: [16]*. b) image of the 316L + V4E with gradient structure sample. Source: author image*

It must be said that on Figure 9 b), the region where the nanoindentation tests were performed is visible – being the shiny squares and scratch indicated with the blue square -.

3.2. Microstructurally tailored materials

3.2.1. 316L manufactured by layer remelting

These samples have been manufactured using three different scanning strategies with additional melting of already solidified layers. This strategy in manufacturing is also called layer remelting.

Essentially, the beam parameters are manipulated in different zones of the component every layer, so that it three-dimensional material microstructure engineering is allowed, as the material microstructure depends on parameters such as solidification rates and thermal history of solidified layers, among others [15].

The parameters were manipulated assigning different strategies in selected zones of the components, as shown in the concentric cones of Figure 10. By doing this, different microstructures are generated in each part of the specimen, and the sample is here analyzed in two cuts effected in the midpart of the specimen; an XY cut (Figure 11 a) and a Z cut (Figure 11 b). Corresponding optical micrographs of each of the cuts previous to the nanoindentation tests are presented in Figures 11 c and d respectively, where the details of the microstructure can be observed in specific areas of the specimens.

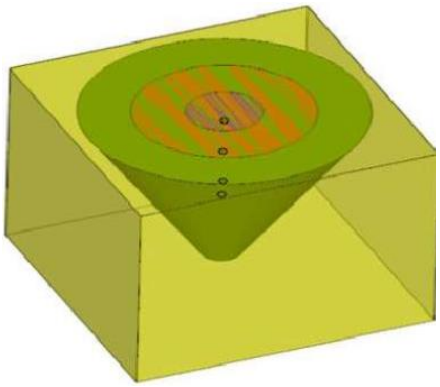

Figure 10: Schematic representation of composition structure for the layer remelting type samples. Source: [15].

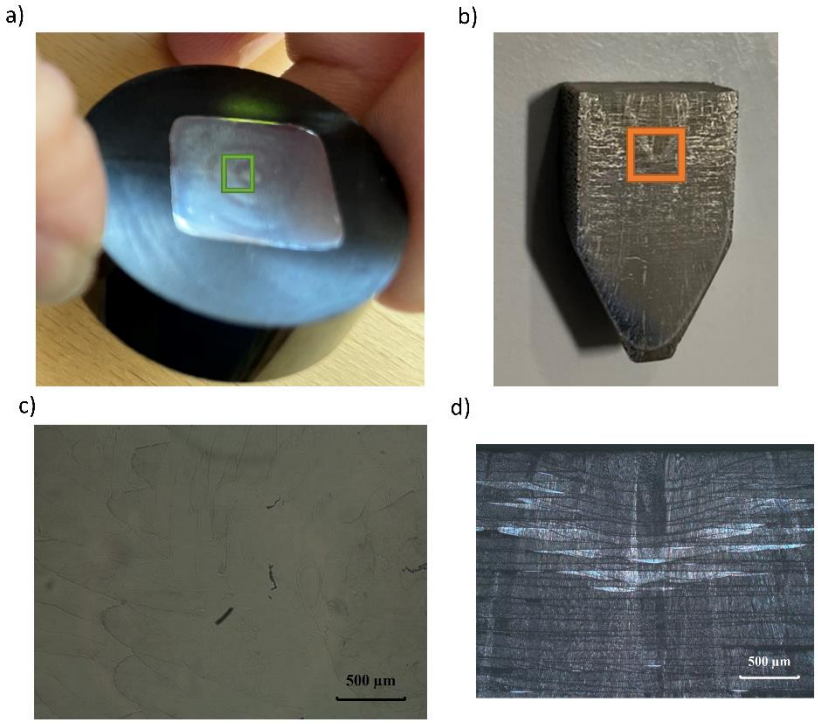

Figure 11: a) 316L axial view sample made by layer remelting. b) 316L axial transversal sample made by layer remelting. c) Optical micrograph of the green square of image a). d) Optical microstructure of the microstructure of the orange square of image b). Source: Carlos Botero.

3.3. Multiphase and composite materials

3.3.1. Super Duplex steel

Microstructure of the super duplex steel sample is shown in Figure 12. Ferritic (α), austenitic (γ) and sigma (σ) phases are expected to be seen [10], but only the ferritic – corresponding to the darkest regions - and austenitic – corresponding to the clearest regions - can be clearly identified with the SEM image taken [80]. However, sigma phase seems to be barely visible (see Figure 12).

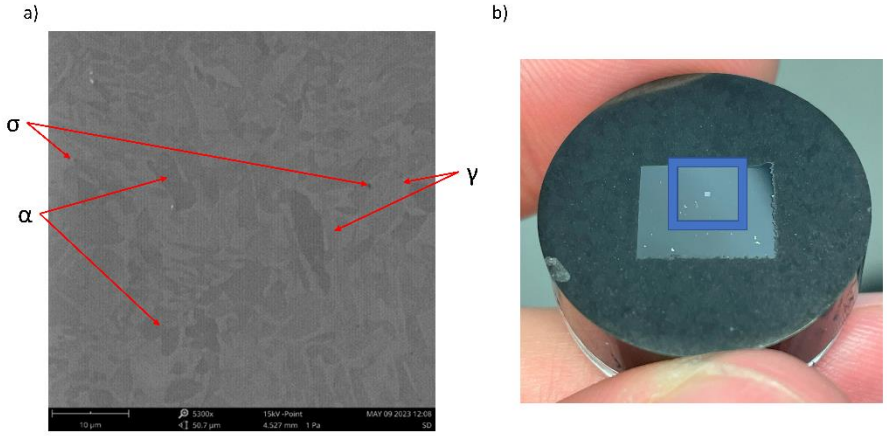

Figure 12: a) SD 2507 steel microstructure, with ferritic (α), austenitic (γ) and sigma (σ) phases indicated by red lines. b) SD sample. Source: author image.

The area indented is delimited with the blue square on Figure 12 b) and can be identified as a shiny square.

3.3.2. 316L + BN

This sample contained two parts, consisting of one bigger than the other, as it can be observed on Figure 13 b). The material is the same, but the small part was cut following the XY manufacturing plane, while the big one was cut following the Z plane - similar to the 316L manufactured with layer remelting case -.

As it happened with the other samples, the indented area is clearly visible as a shiny square. In Figure 13 b) these areas are marked with blue squares. The microstructure is represented on Figure 13 a).

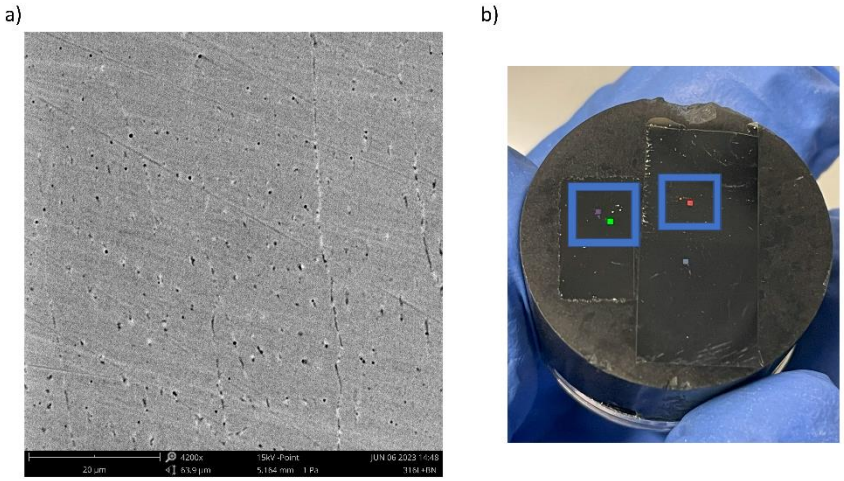

Figure 13: a) microstructure of the 316L+BN sample. b) 316L+BN sample, including the big and small part. Source: author image.

4. Experimental methodology

In this section, all experimental procedure is described, including sample preparation, nanoindentation tests and statistical methods application.

4.1. Sample preparation

All samples were subjected to a meticulous sample preparation procedure to reach the better surface quality as possible to get the most reliable results.

This procedure is formed by three stages: putting the samples in bakelite, grounding and polishing. To put the samples in bakelite, an approximate quantity of 10 ml of conductive bakelite powder was introduced on Struers Labopress-3 machine. 10 mN force and 5 minutes time for the heating and cooling stages were set. The grounding process was done using the Struers Rotopol-31 machine and the 1200 µm grammage polishing paper for 10 minutes with water, as the samples were already grounded and, therefore, the surfaces presented low quantity of defects. The polishing process was done using the Struers Rotopol-31 machine too, and the 6 µm, 3 µm and 1 µm cloth disks for 20 minutes each one and using his respective rough particles and lubricant. For all the steps, the sample position has been changed 90 degrees every 1 or 2 minutes to ensure the efficiency of the sample preparation.

All the described preparation procedure was performed on all the samples, but for the super duplex 2507 one an additional polishing procedure was applied due to the need to perform EBSD analysis, as this type of analysis requires a high-level sample preparation. The final polishing stage was performed using the Vibromet machine, which polish the samples with OPS colloidal silica in an automated way to be sure that the surface will be completely free of any defect.

4.2. Microscopy characterization

SEM, EDS and EBSD were used to analyze and characterize the samples. SEM Phenom XL was used to obtain the SEM images of microstructure and nanoindentations. SEM Zeiss Neon40 equipped with EDS Oxford was used to element analysis. SEM JEOL JSM-7001F equipped with Oxford EBSD was used for the EBSD analysis operated at 20kV with a step size of 0.1 µm.

4.3. Sample placement

The first step before carrying out the nanoindentation tests is to accommodate the samples on the nanoindenter. This is extremely important because a bad accommodation could lead to failed tests or, in a more extreme situation, the tip break. To avoid this, the following considerations has been considered:

- If the sample is not completely flat, it must be embedded in bakelite. This ensure that the sample, indeed, is totally flat and the tests will be performed correctly. If the sample has a small slope, the tests will stop automatically before finishing due to the null detection of the surface. Another possibility is that the tip could scratch the surface and thus the tip could break or wear out, hence affecting the whole results.
- The sample must not exceed the holder height. The compliance of this condition is extremely important: otherwise, the tip will break for sure.
- The bakelite height must be approximately 1 cm. If the actual heigh is greater than the limit, the previous condition will not be fulfilled because the sample will stand out the holder height.

4.4. Nanoindentation tests

Nanoindentation tests were performed in load control using iMicro nanoindenter (KLA) equipped with a diamond sharp Berkovich tip.

4.4.1. Types of tests performed

There are two types of tests with distinctive features. Hence, the selection between these will depend on whether you want to obtain the intrinsic mechanical properties – in which case, the dynamic tests are the optimal – or maps representing the changes in the mechanical properties – in which case, Nanoblitz tests must be chosen -.

4.4.1.1. Dynamic tests

This type of tests consists in measuring the hardness and the elastic modulus continuously while the nanoindentation is being performed. The main objective is to determine the intrinsic properties of the material.

In dynamic tests matrices of indentations are made, and each corresponds to a test. It is possible to choose dimensions, but in this study is assumed that 3x3 are enough to achieve the objective.

Once the dynamic test is finished, an average value for hardness and another for modulus, with its standard deviation, is obtained for every single test and for the total amount of tests performed. Additionally, it is possible to get hardness or elastic modulus in function of penetration depth graphs.

Dynamic tests are useful, for example, to analyze the property changes in heterogeneous materials that present composition gradient.

4.4.1.2. Nanoblitz tests

Nanoblitz tests differs from the dynamic ones by the fact that the hardness and elastic modulus are not measured continuously, but a greater number of tests are performed. This is because the objective is to represent how the mechanical properties – specifically the hardness and the elastic modulus - change through map-style representations.

This type of test is of great interest as it makes possible to correlate the mentioned mechanical properties with microstructure images taken by SEM.

4.4.2. Tests conditions

The test conditions include multiple parameters that are extremely important because an incorrect determination of it may lead to incorrect results, due to the apparition of ISE or pile-up or sink-in, among others. To avoid these undesirable effects, an optimal selection of depth and spacing between indents must be chosen.

To determine the test conditions, a trial test should be made on the sample which conditions we want to find establishing a parameter called decremental. Its function is to gradually lower the target load of the test. The aim to do this is to find the optimal load at which the spacing would be 10 times the depth value.

It is very important to clarify that one sample could have more than one test condition if it contains clearly differentiated sections (for example, an etched sample). Therefore, the number of trial tests should vary depending on the studied sample.

4.4.2.1. Finding the optimal test conditions

Inview Review Data software is needed to properly determine the test conditions of the sample to be tested. Three graphs should be created from the data obtained through the trial test:

- Modulus vs X position
- Load vs X position
- Load vs depth

On the first graph, modulus is mostly constant in function of X position, but from certain X position, modulus begins to change, either by increasing or decreasing. This X position should be remembered.

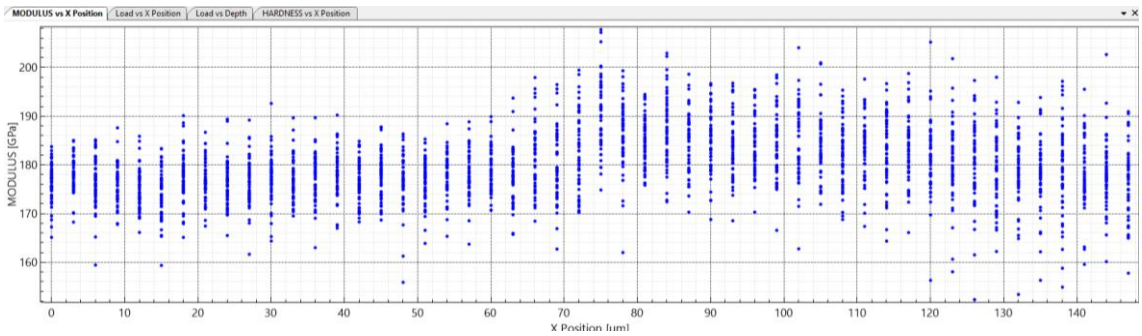

Figure 14: Modulus vs X position graph example. Modulus values changes, approximately, on X position = 60 µm. Source: author image.

On the second graph, target load is determined by the X position determined from the previous graph.

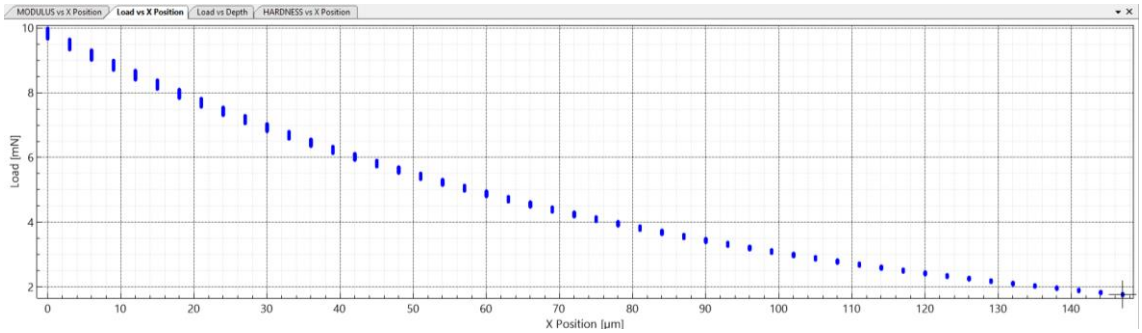

Figure 15: Load vs X position example. For X position = 60 µm, its load is 5 mN, approximately. Source: author image.

On the last graph and using the load obtained, an estimated value for depth is achieved. Now, the spacing rule can be applied to know the spacing between indents.

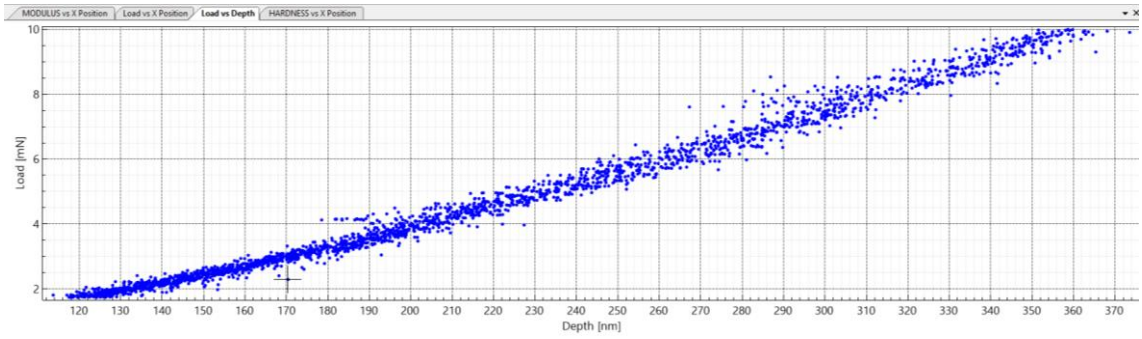

Figure 16: Load vs depth graph example. For 5 mN load, 230 nm depth is estimated. Source: author image.

Knowing these parameters, dimensions of the maps and number of indents (points) can be established ensuring that the resolution will be the maximum as possible.

4.5. Tests performed

4.5.1.1. 316L + V4E with transition structure

Nanoblitz maps with different dimensions were done on every sample region: two corresponding to the 316L region and two on the V4E region.

On the 316L region, maps with 150 x 150 µm dimensions were done with 5 mN load indentations with 2.3 µm spacing between them (65 x 65 indentations). On the V4E region, the load was 4.5 mN and spacing 1.7 µm. Maps with 400 x 400 µm were realized with the same load and spacing (173 x 173 points).

On the V4E region, 150 x 150 µm maps were effectuated applying 4.5 µm load and maintaining 1.7 µm spacing (88 x 88 indentations). 400 x 400 µm maps consisted in the same load and spacing (235 x 235 indentations).

4.5.1.2. 316L + V4E with gradient structure

A total number of 14 Nanoblitz tests were done throughout the sample. The main intention was to see how properties changed through the gradient between the two metals that constitute the sample.

Every map had 200 x 400 µm dimensions with 20 x 40 indents, resulting in a spacing of 10 µm, and load was set to 10 mN. Therefore, the total number of indentations was 11200. In this case, the optimal tests conditions were not searched because performing this test with maximum resolution would take an exorbitant amount of time. The main objective was, therefore, to visualize how the properties changes throughout the gradient in a general approach.

As it has been seen that there are specific regions with a high number of molybdenum - and vanadium - rich carbides in V4E, 7 additional maps were taken place in that regions to analyze the carbide distribution. In this case, as maximum resolution as possible is needed, optimal test conditions were found, which have turned out to be 2.5 mN load and 3 µm spacing. Dimensions of each map were 200x150 µm, which implies 23334 indentations in total.

After the nanoindentation maps were realized, EDS analysis of the composition was performed.

4.5.1.3. 316L manufactured with layer remelting

The same concatenation of Nanoblitz maps as the one realized in 316L + V4E with gradient structure were performed on this samples, as the objectives are the same: see how the properties changes through a large area.

The maps had 200 x 400 µm dimensions with 40 x 60 indents, which implies 5 µm spacing and 33600 indentations in total. It was decided to increase the maps resolution basing on the time needed to finish the tests made on the in 316L + V4E with gradient structure sample, which turned out to be lower than expected.

4.5.1.4. Super Duplex 2507

This sample was analyzed using SEM, EBSD and nanoindentations techniques. The main objective was to correlate the SEM and EBSD images, and the SEM image with the hardness nanoindentation map.

A single 400x400 Nanoblitz map was done on this sample. After doing the optimal test conditions finding procedure, 3.5 mN load with 1.5 µm spacing was set up.

4.5.1.5. 316L + BN

Two different dimensions were used to perform the Nanoblitz maps on each part of the sample: 150x150 µm and 400x400 µm. The optimal test conditions obtained were clearly different for the bigger part and for the smaller, consisting of 5 mN load with 2.1 µm spacing for the bigger part, and 2 mN load with 1.2 µm spacing for the smaller one. Nevertheless, it was decided to consider a safety factor for the spacing parameter to ensure that the results were not altered by the overlapping effect. Therefore, the spacing was set up to 2.5 µm and 1.5 µm, respectively, which implies 3600 indentations for the 150x150 µm maps and 25600 for the 400x400 µm on the big part, and 100000 indentations for the 150x150 µm maps and 70756 for the 400x400 µm on the small part.

4.5.1.6. 316L reference

As in the 316L + BN sample, 150 x 150 µm and 400 x 400 µm dimensions were used to make the Nanoblitz maps. The optimal test conditions found to be 4.5 mN load with 2.3 µm spacing. As the 316L + BN sample, a safety factor was considered on the spacing parameter, that was finally set up to 2.5 µm. Therefore, 3600 indentations constituted the 150 x 150 µm maps and 25600 the 400 x 400 µm ones.

It is important to note that the dimensions of the maps performed are chosen depending on the sample surface quality and the time available to the results obtaining. Also, the feature high parameter was set to 700 nm in all tests to ensure that no scratching is produced by the tip indenter.

5. Results and discussions

In the following chapters all results obtained of every sample in the study and the discussion are compiled, including contour plots and data deconvolution using GMM clustering.

5.1. Multilayered materials

5.1.1. 316L + V4E transition characterization

In Figure 17 a) it can be seen the microstructure of the sample. Large and columnar austenite grains can be identified on the lower part of the image - that corresponds to the 316L steel region -, while on the top part of the image these grains lose its characteristic elongated shape – this region belongs to the V4E region, with Mo and V rich carbides. In the b) image, an EBSD image is shown, and different crystallographic orientations for the austenite grains are indexed.

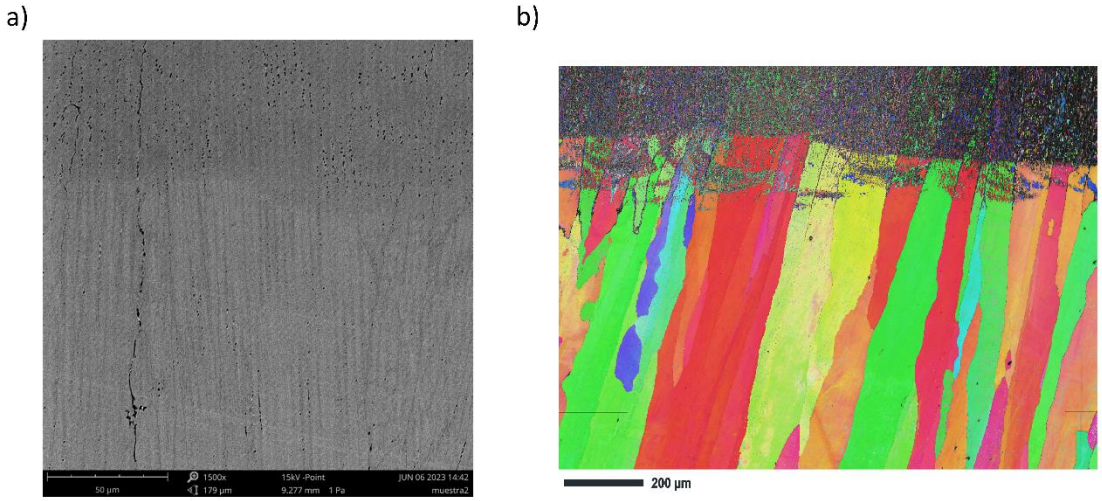

Figure 17: a) SEM image of the 316L+V4X with transition structure microstructure. b) EBSD image of the transition between the 316L and the V4E regions. Source: author image.

Figure 18 contain the hardness and modulus contour plots obtained through the Nanoblitz tests of the 316L region of the sample, corresponding the a) and b) images to the 150x150 µm maps, and c) and d) to the 400x400 µm ones. The austenite grains are clearly visible on the big dimensions maps, especially in the d) image.

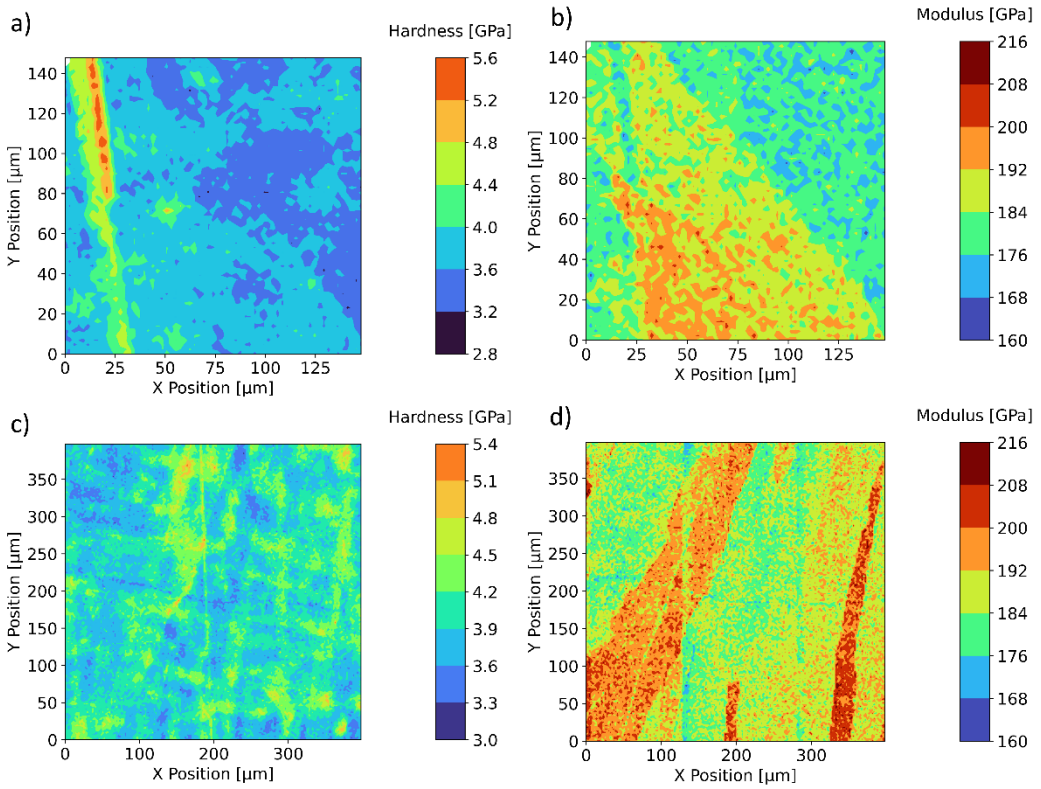

Figure 18: Contour plots of the 316L region of the 316L+V4E sample with transition structure. a) and b) maps have 150x150 µm dimensions, whether c) and d) have 400x400 µm dimensions. Source: author image.

As it is known that only austenite phase is present in 316L steel [9], [48], the variations on the elastic modulus values – where it can be thought that these represent two different phases – are caused by the differences in crystallographic orientations. Regarding the hardness contour maps, the fact that the crystallographic orientations are not as clear as for the elastic modulus ones must be highlighted.

On the d) image, there are two different crystallographic orientations – that corresponds to the elongated columnar grains -, one having a modulus between 192 and 224 GPa, and the other between 160 and 192. On the b) image it is possible to see a more detailed region of the transition between the two crystallographic orientations.

Statistical analysis is performed using the GMM clustering algorithm. Figure 19 compares the obtained X vs Y position cluster plot with the modulus contour plot. The large columnar austenite grains can be seen containing two different crystallographic orientations.

In Figure 20, contribution of each identified cluster is represented above the experimental data histogram. In Figure 21, the hardness vs modulus cluster plot is presented, showing a high-level of dispersion of the crystallographic orientations 1 and 4 clusters.

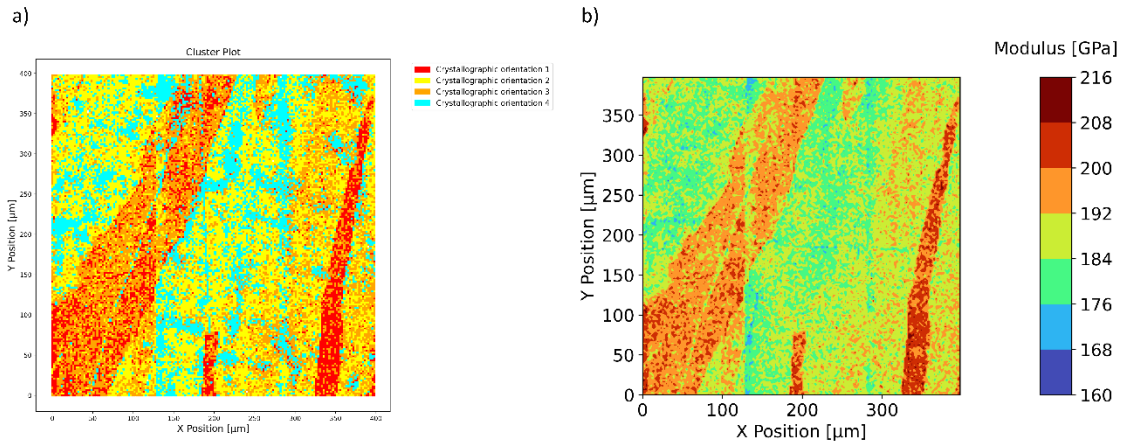

Figure 19: comparison between a) the X position vs Y position cluster plot and b) the modulus contour plot of the316L region of the 316L+V4X transition sample. Source: author image.

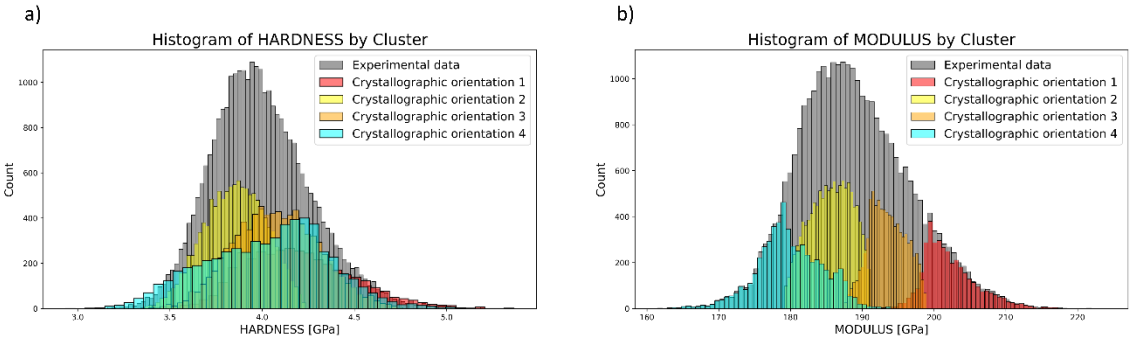

Figure 20: contribution of each cluster of the 316L region of the 316L+V4E transition sample. Source: author image.

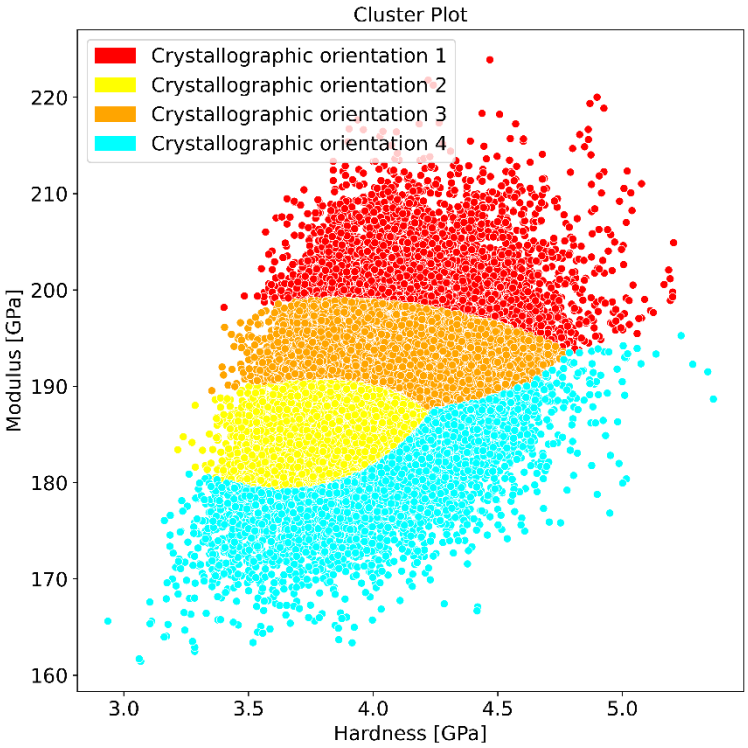

Figure 21: hardness vs modulus cluster plot of the 316L region of the 316L+V4E transition sample. Source: author image.

From the Figure 19 it can be said that the similarity between the cluster and contour plots is extremely high, indicating that the algorithm is able to detect and classify into clusters the nanoindentation tests data. Nevertheless, in Figure 20 is possible to see that the contributions of each clusters overlap each other, indicating that these does not fit completely fine to the experimental data, which could mean that there are some uncertainties on the clustering – which seems that is not the case, as the cluster and contour plots are very similar each other -. Also, it must be highlighted the fact that the cluster contributions fit better on the modulus values than on the hardness. From the Figure 21, it can be deduced that the crystallographic orientations 2 and 3 clusters are the ones with higher grade of adjustment, as the data dispersion is low, and the 1 and 4 ones involve uncertainty because of the data dispersion – which possibly is caused by the overlapping with the other contributions (see Figure 20 b)).

Figure 22 includes the hardness and modulus contour plots, obtained thanks to the nanoindentation maps, of the V4E region of the sample. The Mo and V rich carbides can be seen in a) and b) images, while surface defects – with also the Mo and V rich carbides - are visible in c) and d) images.

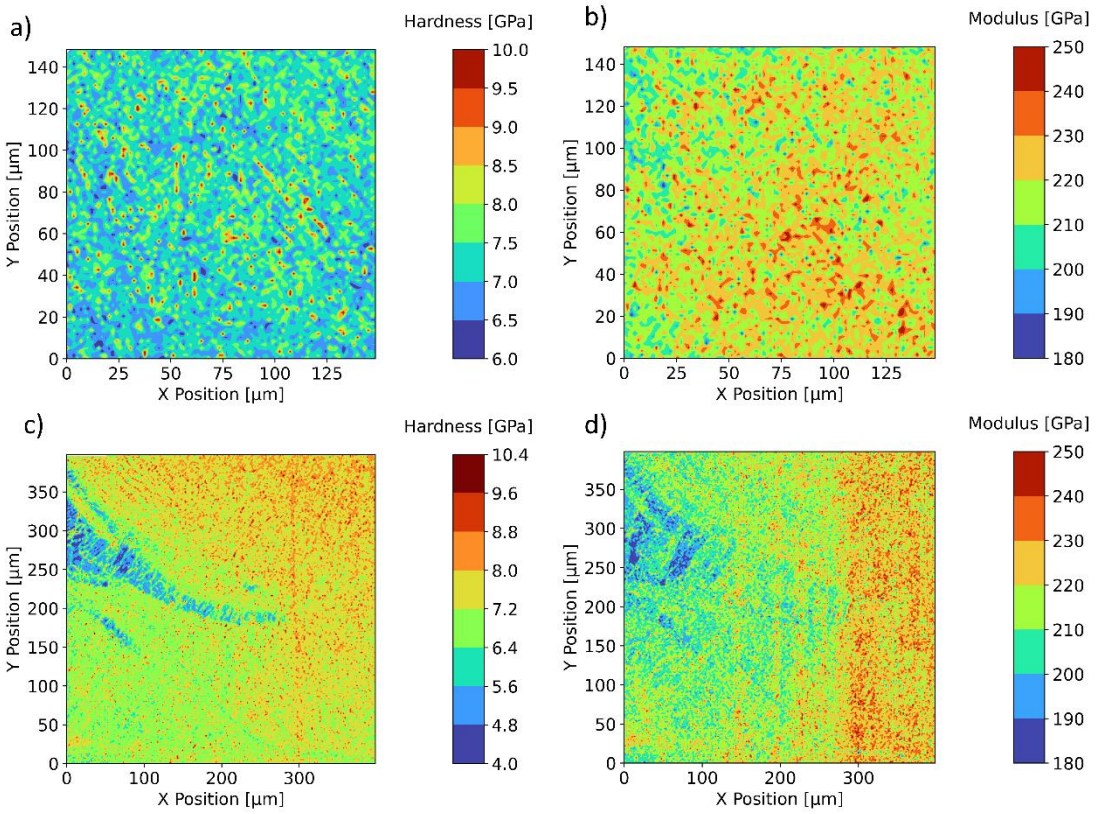

Figure 22: contour plots of the V4E region of the 316L+V4E transition sample with transition structure. a) and b) maps have 150x150 µm dimensions, whether c) and d) have 400x400 µm dimensions. Source: author image.

Figure 22 a) and b) images provide us a well-defined image of the present microstructural phases, which can be speculated that are martensite, retained austenite, and carbides [11], [12]. As the carbides are the hardest phase, they are clearly identified as red dots, having hardness values between 9 - 12 GPa. On the other hand, the retained austenite and martensite are discerned with light blue and green areas, having hardness values between 5 - 7 GPa, and 7 – 9 GPa, respectively. The phase distribution seems to be homogeneous, with the absence of any texture. Looking at Figure 22 c), it is possible to see a very soft region – relative to the other values – represented with dark blue color. This corresponds to a surface defect. On the top of the plot there is a well-distributed carbide region, that seems to have the same structure that the one observed in Figure 22 a).

Looking at Figure 22 d), it is evident that the equipment has measured inaccurate values for the elastic modulus, as we can see an abrupt change in X position, which seems not to be related to the microstructure. A notable observation is that surface defects significantly impact the measured mechanical properties, as evident from the contour plots. With this, it has been detected that elastic modulus is sensitive to minor changes that may occur during the test, and it is not possible to provide a clear explanation for this behavior. Therefore, we may not consider the modulus presented as a

reliable indicator of the material's true elastic modulus. Instead, it is presented as an additional characteristic associated with the sample.

The statistical analysis for the V4E region of the 316L+V4E have been done using the 150x150 µm contour maps data due to the presence of surface defects on the 400x400 µm ones, that may affect negatively on the phase identification. In consequence, the data amount to analyze is lower.

In Figure 23, a comparison between the X vs Y position cluster and contour plots is presented. Figure 24 shows the cluster contribution of each cluster – named with the speculated phases present on the material -, and Figure 25 shows the hardness vs modulus contour plot.

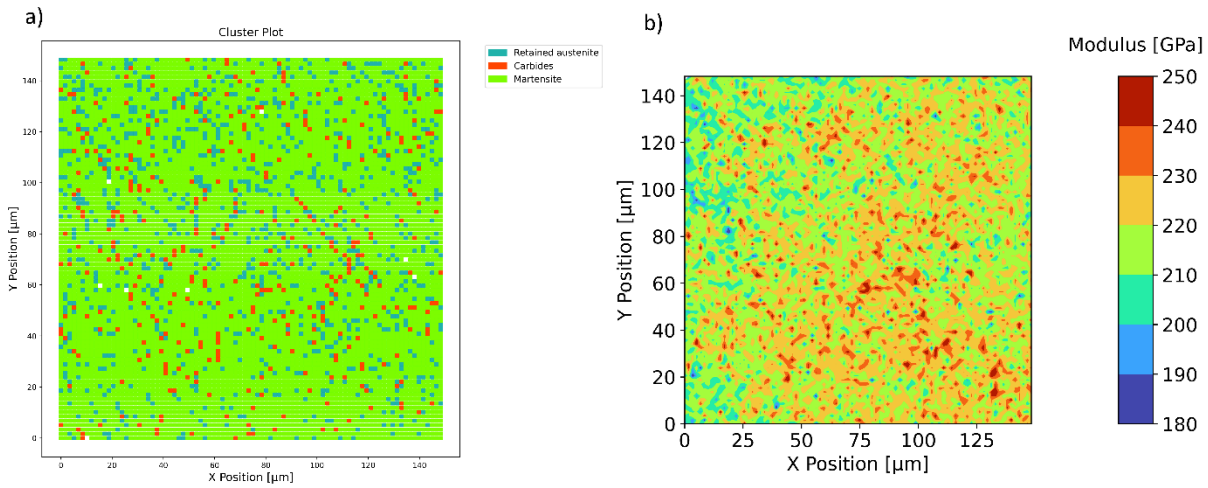

Figure 23: comparison between a) X position vs Y position cluster plot and b) X position vs Y position contour plot for the V4E region of the 316L+V4E transition sample. Source: author image.

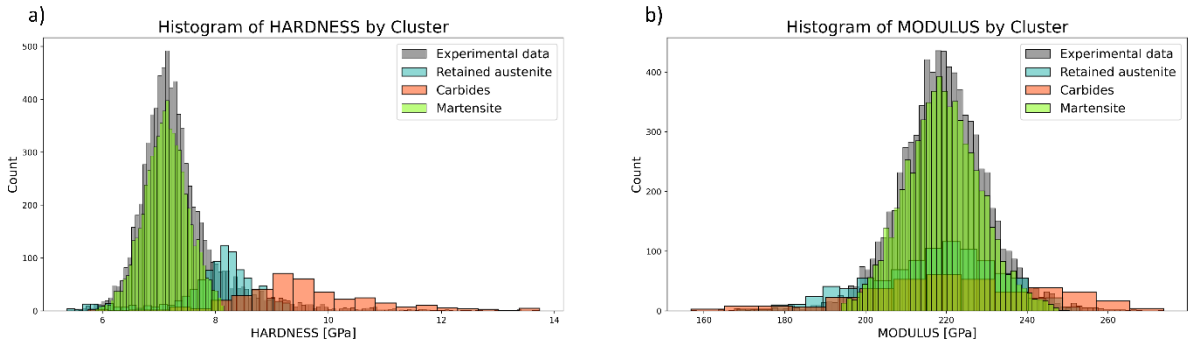

Figure 24: contributions of each cluster of a) hardness and b) elastic modulus for the V4E region of the 316L+V4E transition sample. Source: author image

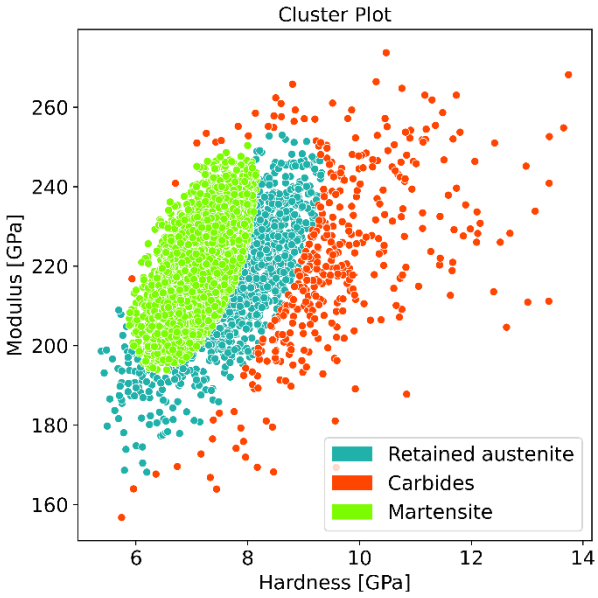

Figure 25: modulus in function of hardness representation of the phases identified by the clustering algorithm for the V4E region of the 316L+V4E transition sample. Source: author image.

Comparing the clustering and the contour plot of hardness in X and Y position we can see that the clustering has not fitted well the data (see Figure 23). In the contour plot it is clearly observed three regions: blue (180-200 GPa) which may correspond to austenite, green (200-230 GPa) which may correspond to martensite and red (230-250 GPa) which may correspond to the carbides. This is because the values of hardness of the phases austenite and martensite are very close, and the method is not fitting this well. Therefore, a future work must be done focusing in improving this clustering. Nevertheless, looking at the contributions of the clusters identified by the algorithm (Figure 24), the martensite one fits almost perfectly to the experimental data, while the carbides and retained austenite clusters not.

Analyzing the Figure 25 cluster plot, the data dispersion of the carbides cluster is quite considerable. On the other hand, martensite cluster is well-defined, matching with the fact that its associated data fits almost perfectly with a gaussian distribution.

5.1.2. 316L + V4E sample with gradient

Figure 26 presents the 14 hardness contour plots concatenated, resulting in a single big-dimensional map of 6000x150 µm. The arrows point to areas containing Mo and V rich carbides – from the layers of V4E -, subsequently analyzed in more detail.

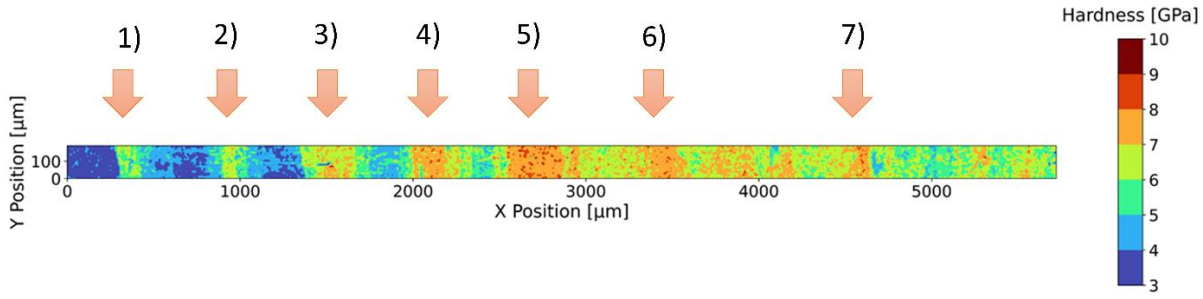

Figure 26: Concatenation of the 14 hardness contour plots. The arrows point to the approximate area in which a more detailed contour plot has been done subsequently. Source: author image.

As the X position increases, more V4E layers are mixed with the 316L steel, and the hardness of what turned out to be 316L increase progressively.

In Figure 27, the detailed hardness contour plots and EDX of the pointed areas showed on Figure 26 are exposed.

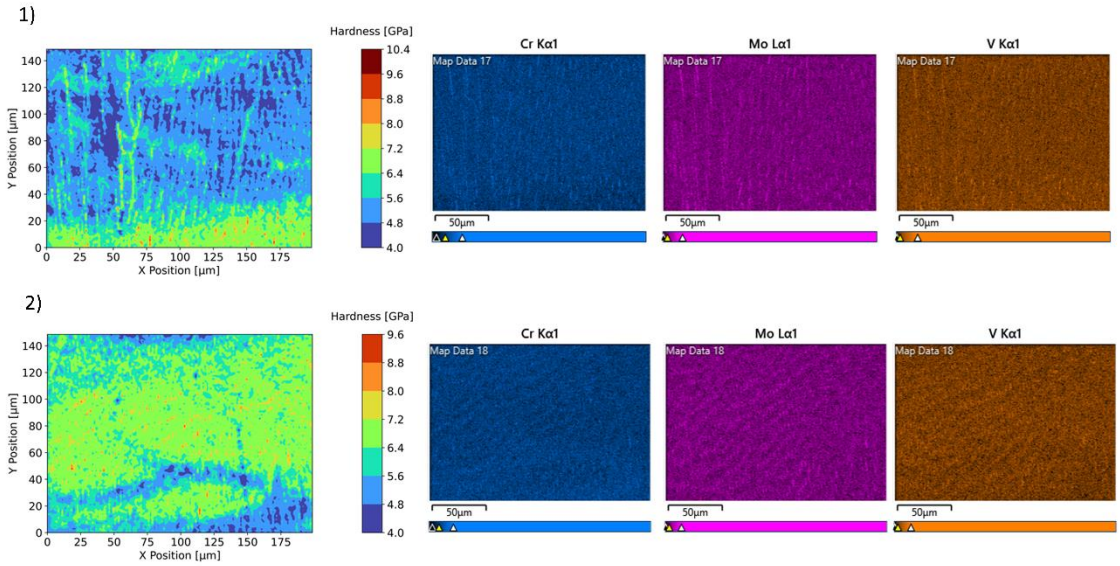

3)

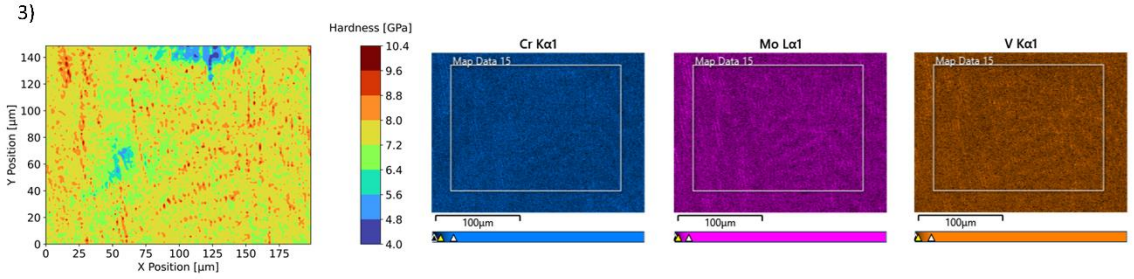
Hardness [GPa]
10.4
9.6
8.8
8.0
7.2
6.4
5.6
4.8
4.0
Cr Kα1
Mo Lα1
V Kα1
Map Data 15
100µm
Y Position [µm]
X Position [µm]
0 25 50 75 100 125 150 175
0 20 40 60 80 100 120 140

4)

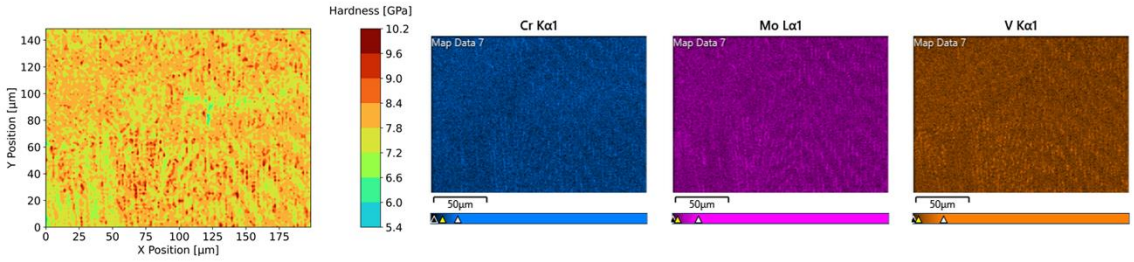
Hardness [GPa]
10.2
9.6
9.0
8.4
7.8
7.2
6.6
6.0
5.4
Cr Kα1
Mo Lα1
V Kα1
Map Data 7
50µm
Y Position [µm]
X Position [µm]
0 25 50 75 100 125 150 175
0 20 40 60 80 100 120 140

5)

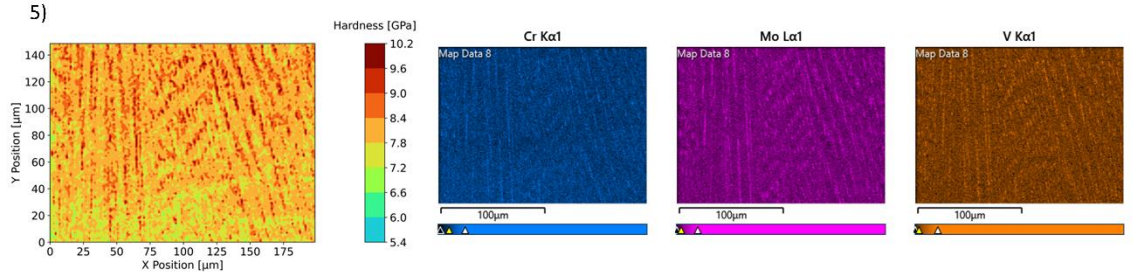
Hardness [GPa]
10.2
9.6
9.0
8.4
7.8
7.2
6.6
6.0
5.4
Cr Kα1
Mo Lα1
V Kα1
Map Data 8
100µm
Y Position [µm]
X Position [µm]
0 25 50 75 100 125 150 175
0 20 40 60 80 100 120 140

6)

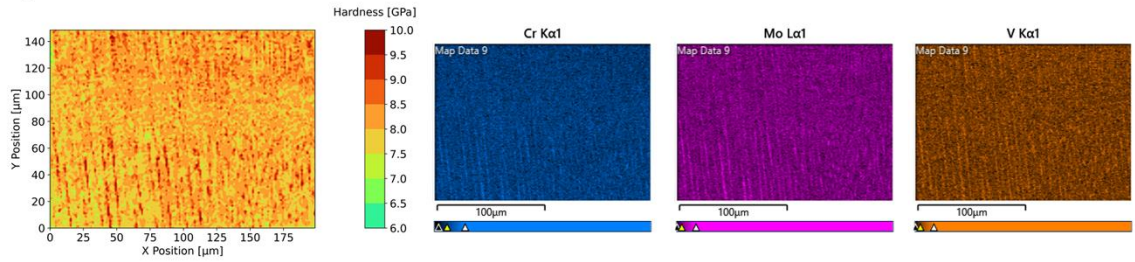
Hardness [GPa]
10.0
9.5
9.0
8.5
8.0
7.5
7.0
6.5
6.0
Cr Kα1
Mo Lα1
V Kα1
Map Data 9
100µm
Y Position [µm]
X Position [µm]
0 25 50 75 100 125 150 175
0 20 40 60 80 100 120 140

7)

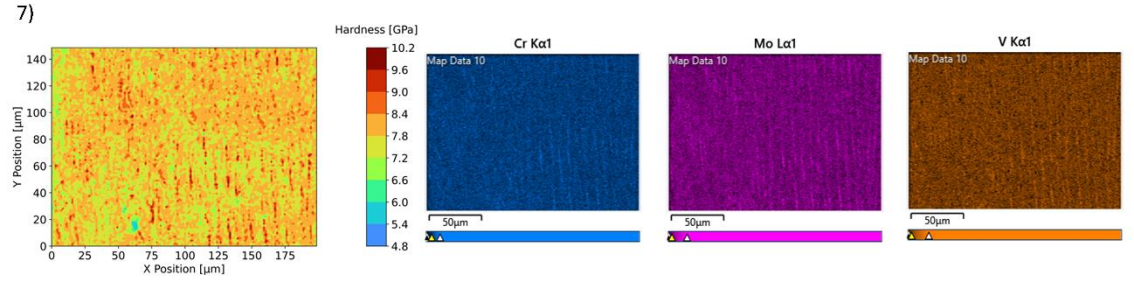
Hardness [GPa]
10.2
9.6
9.0
8.4
7.8
7.2
6.6
6.0
5.4
4.8
Cr Kα1
Mo Lα1
V Kα1
Map Data 10
50µm
Y Position [µm]
X Position [µm]
0 25 50 75 100 125 150 175
0 20 40 60 80 100 120 140

Figure 27: Detailed hardness contour plots of the indicated regions in Figure 23, and it's respective EDX maps. Source: author image.

As it is expected because of the Figure 26 contour plot, the number of carbides - represented in red -, increases as we go along the X position, and slightly decreases on the last test. These carbides reach hardness values of 9-10 GPa and are disposed in an elongated form.

The results of the EDS tests allow us to verify its chemical composition. Also, if we compare it with the contour plots, we can realize that they match perfectly. This allows us to state that, effectively, the red zones represented in the contour plots are the expected Mo and V rich carbides.

In Figure 28 is presented the same map style as previously showed in Figure 26 but using the elastic modulus values. The Mo and V rich carbides areas are pointed with arrows and matches with the ones marked in the hardness contour plot.

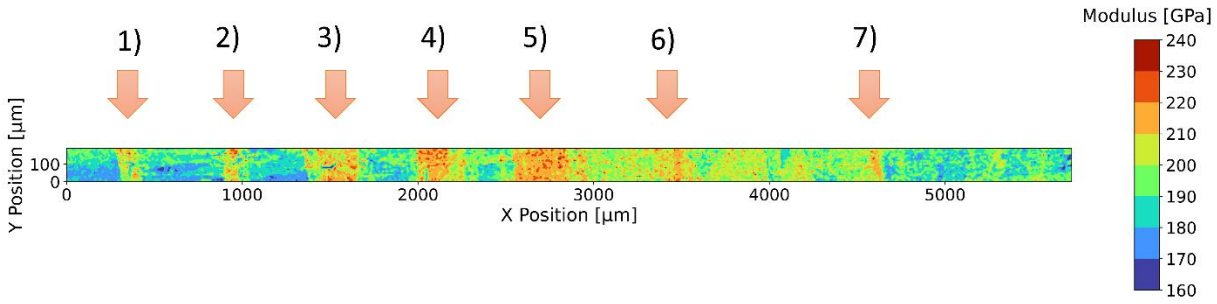

Figure 28: Concatenation of the 14 modulus contour plots. The arrows point to the approximate area in which a more detailed contour plot has been done subsequently.

In Figure 29, the elastic modulus contour plots with its corresponding EDS images are presented.

1)

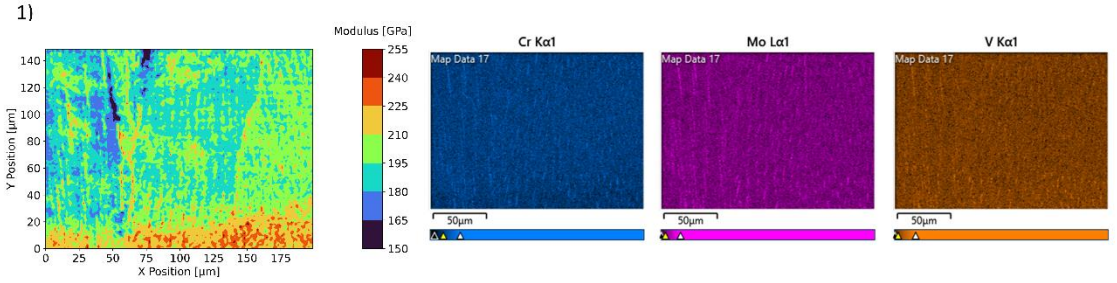
Modulus [GPa]
255
240
225
210
195
180
165
150
Cr Kα1
Mo Lα1
V Kα1
Map Data 17
Y Position [µm]
X Position [µm]
50µm

2)

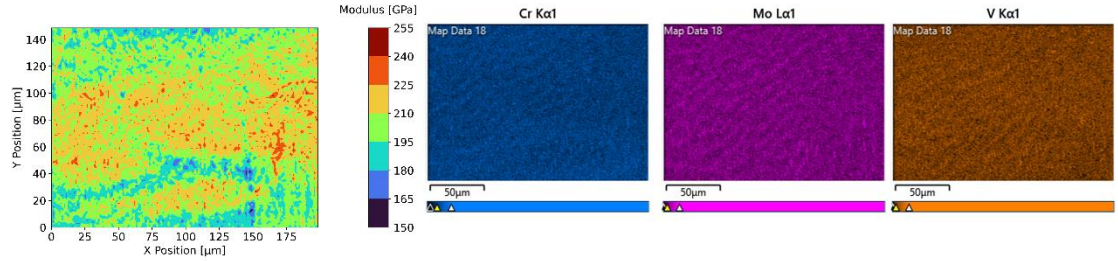
Modulus [GPa]
255
240
225
210
195
180
165
150
Cr Kα1
Mo Lα1
V Kα1
Map Data 18
Y Position [µm]
X Position [µm]
50µm

3)

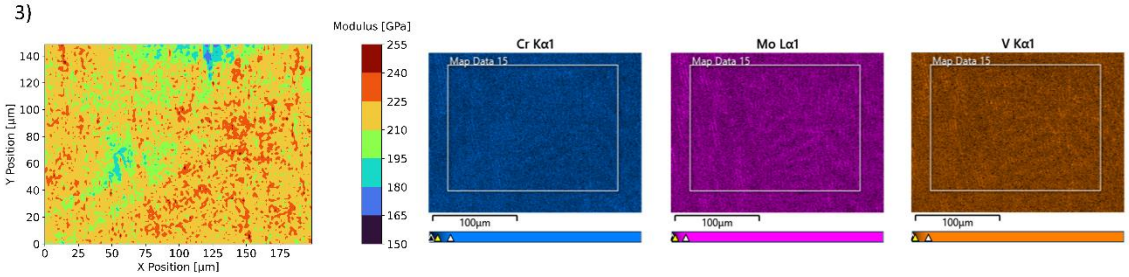
Modulus [GPa]
255
240
225
210
195
180
165
150
Cr Kα1
Mo Lα1
V Kα1
Map Data 15
Y Position [µm]
X Position [µm]
100µm

4)

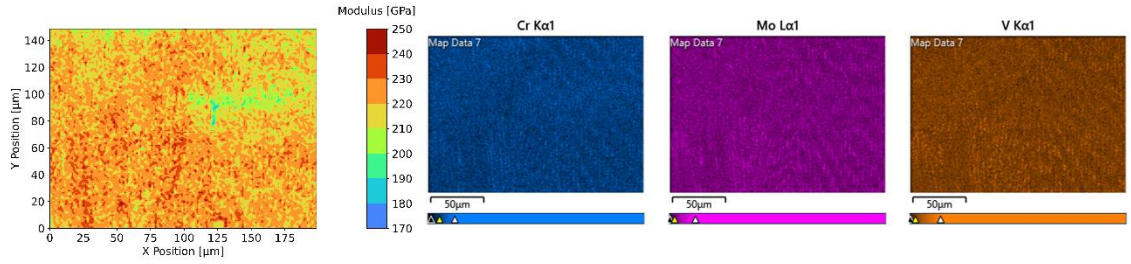
Modulus [GPa]
250
240
230
220
210
200
190
180
170
Cr Kα1
Mo Lα1
V Kα1
Map Data 7
Y Position [µm]
X Position [µm]
50µm

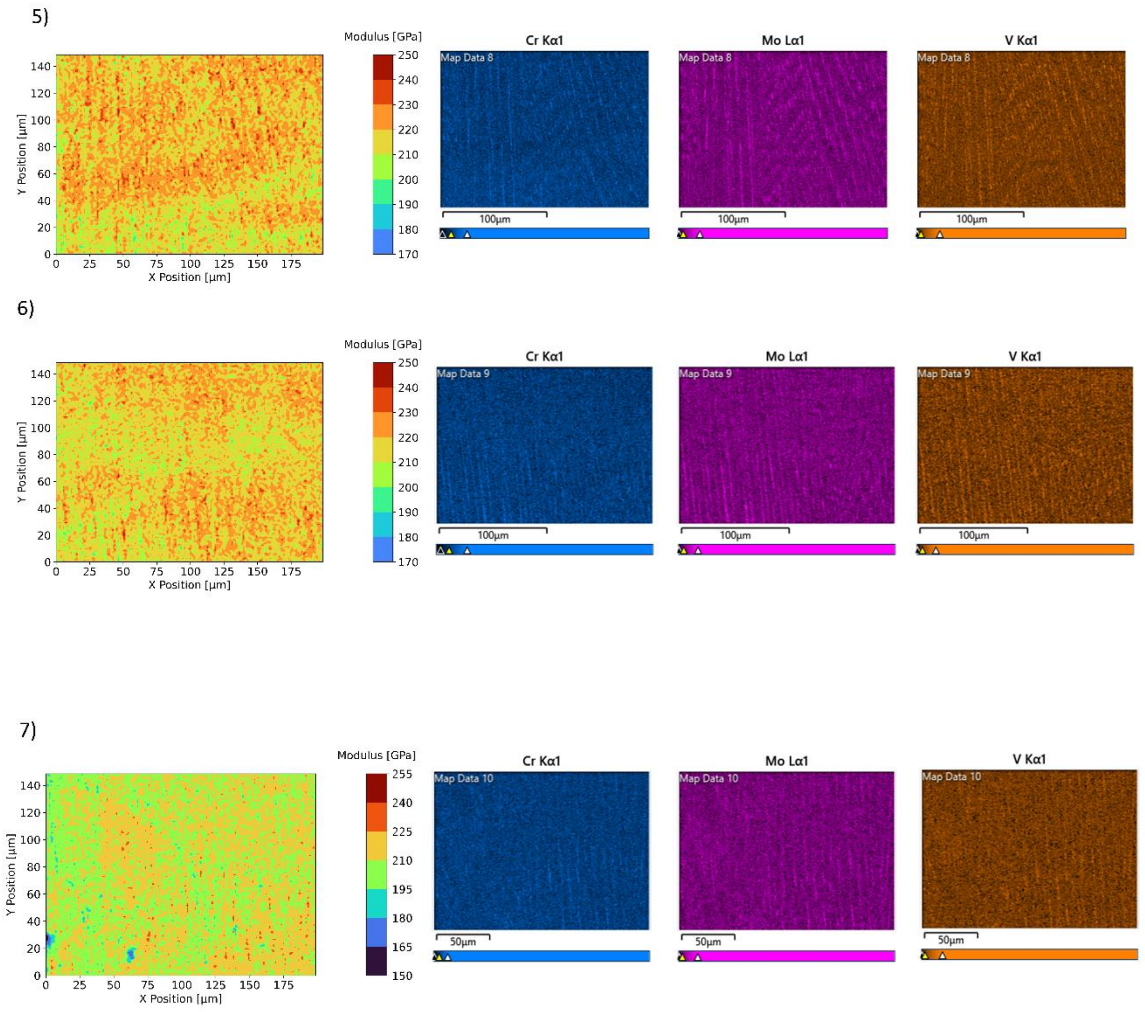

Figure 29: Detailed elastic modulus contour plots of the indicated regions in Figure 21, and it's respective EDX maps. Source: author image.

The EDS results shown in Figure 29 are the same as in Figure 27; they have been shown twice only with the purpose of comparing them with the modulus contour plots. It is interesting to focus on the first plots of Figures 27 and 29 since it can be appreciated a similarity with the contour plot obtained analyzing the 316L+V4E transition sample, concretely the one performed on the 316L region. Furthermore, initial mixture of the V4E carbides with the 316L is clearly captured on these plots.

In Figure 30 a) is represented the trend that follows the presence of the elements Cr, Mo, and V. The b) image shows a more detailed representation of the Mo and V tendency. Both trends are presented as the change in % of elements along X position in the gradient.

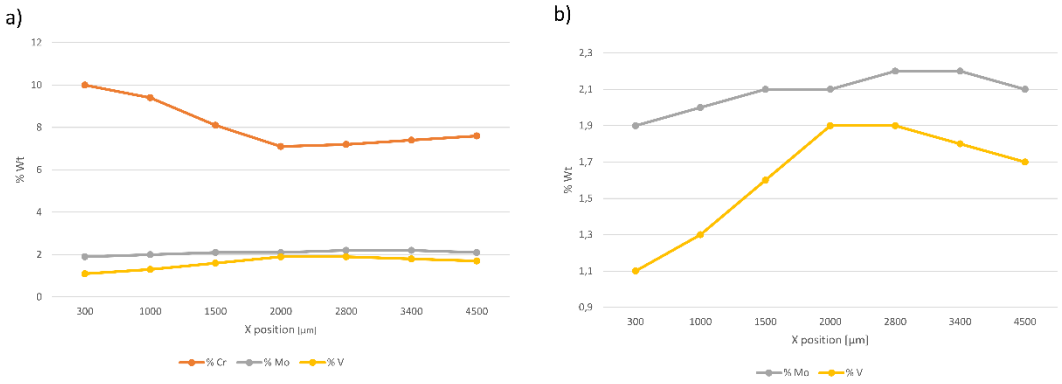

Figure 30: a) carbide presence tendency of the Cr, Mo, and V elements from the Figure 15 maps. b) detailed tendency of the Mo and V elements. Source: author image.

Chromium content - present in higher content in 316L - decreases from 10% to 7.1% meanwhile molybdenum and vanadium increase slightly from 1.9% to 2.2% and 1.1% to 1.9%, respectively, in tests 1 to 4. This phenomenon could be related to the increase in V4E carbides as it is possible to observe an increase of red zones in the contour maps. The 316L steel contains a high quantity of chromium, while the V4E have a high quantity of vanadium, as has been showed previously on Table 1. Therefore, the decrease of chromium and increase of the other elements makes sense, as a high quantity of chromium involves the presence of 316L steel, and high quantity of vanadium involves the presence of V4E, remembering that the sample manufacturing consisted in 316L steel being gradually mixed with V4E. From tests 4 to 7, chromium content increases slightly from 7.1% to 7.6%, while molybdenum and vanadium maintain its values. Again, this makes sense as less quantity of V4E carbides and more 316L steel are observed on the contour plot and considering that the chromium and vanadium content is related with the presence of 316L and V4E steel.

Table 2 compiles all the data graphed in Figure 30 a). The tendency of the molybdenum and vanadium have been represented with more detail on Figure 30 b).

Table 2: percentage in weight values in function of test number from the EDS analysis. Source: author table

Test number	%wt Cr	%wt Mo	%wt V
Test 1	10	1.9	1.1
Test 2	9.4	2	1.3
Test 3	8.1	2.1	1.6
Test 4	7.1	2.1	1.9

Test 5	7.2	2.2	1.9
Test 6	7.4	2.2	1.8
Test 7	7.6	2.1	1.7

Nevertheless, the percentage in weight of the elements obtained through EDS analysis does not coincide with the data from the literature [11], [12]. For this reason, is important to consider that the percentages obtained and mentioned in Table 2 are not representative of the whole sample due to the small area of the tests performed. Also, it should be considered the fact that the main function of the EDS analysis is to see tendencies of the studied elements. Therefore, as the values of the Table 2 does not correspond to the nominal composition of the sample, the non-coincidence of its values and the ones written on the literature is not a problem.

No statistical analysis is applied on this sample since it is constituted by a 316L and V4E steels mixture, giving place to an extra difficulty on the phase's identification or crystallographic orientation process and preventing the correct execution of it.

5.2. Microstructurally tailored materials

5.2.1. 316L sample manufactured with layer remelting

Figure 31 indicates the locations where the nanoindentation maps were performed, and Figure 32 the concatenation and merging of the maps for the samples manufactured with layer remelting of 316L steel. Figure 32 a) refers to the sample that have been cut to make the transversal view visible, and b) to the one with the axial view visible.

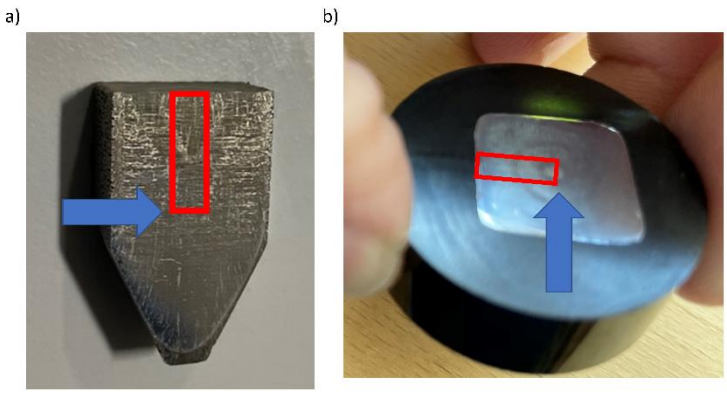

Figure 31: approximate location of the tested areas. The arrow point to the starting point of the maps. Source author image.

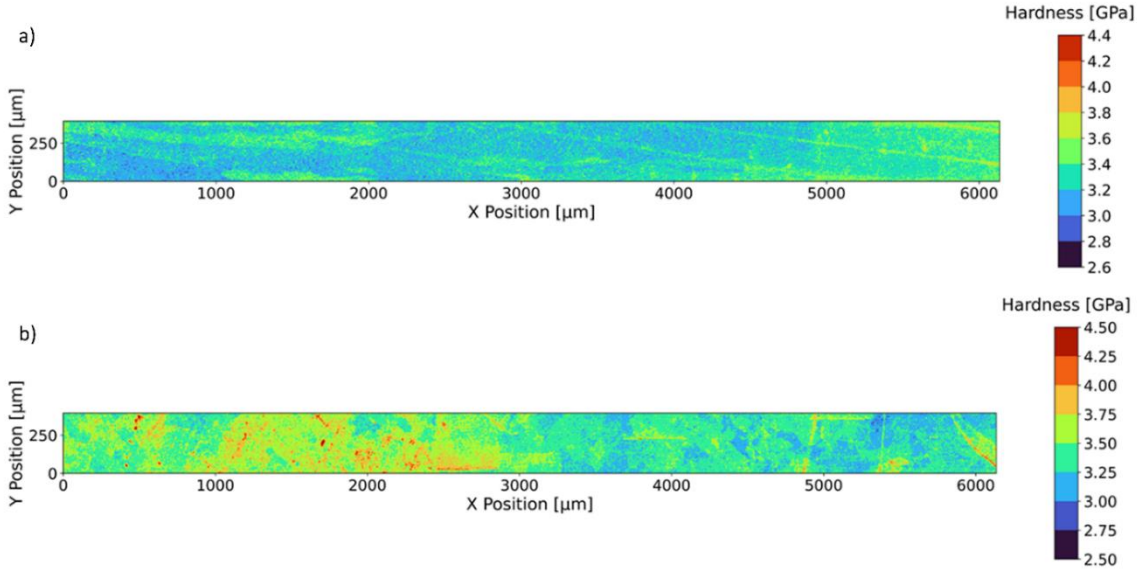

Figure 32: concatenation of the 14 hardness contour plots for a) the transversal view and b) the axial view of the 316L samples manufactured with layer remelting.

Regarding the sample with the transversal view visible, we can observe the elongated grains - as expected - in the manufacturing direction. Two main changes occur at the beginning and at the end of the area, but in general no relevant changes are observed. On the other hand, for the sample tested in the axial view, it can be clearly observed that in the first 3000 µm some carbides are present in the hard phase.

From these two contour plots, it could be said that the regions with different hardness values indicates that microstructural changes may have been taken place, and that the hardness values are more sensitive to it in X and Y position than to the Z one.

In this case, statistical analysis has not been done either. The objective for this part is to report the changes along the different directions and see how laser remelting affects the mechanical properties. Since the phases change along the X axis, clustering analysis does not make sense.

5.2.2. Super duplex steel 2507

In Figure 33, the hardness and modulus contour plots corresponding to the super duplex steel sample are exhibited.

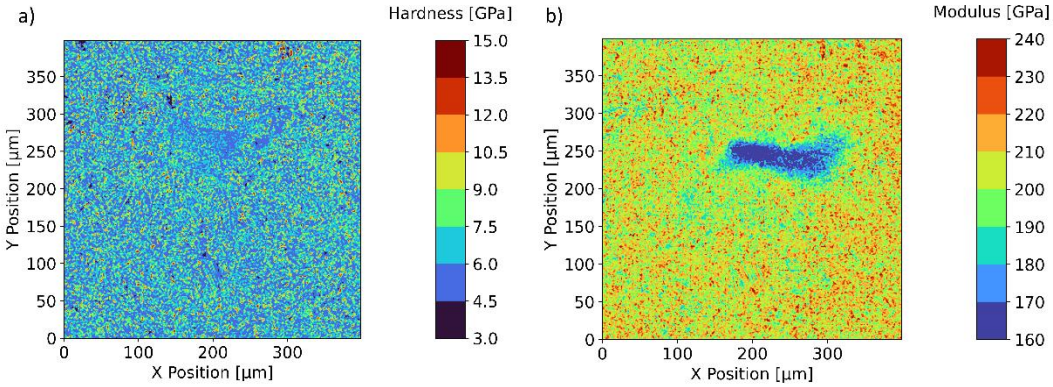

Figure 33: a) hardness and b) modulus contour plots of the nanoindentation map performed on the SD sample. Source: author image.

The microstructure with small grains of sigma, ferrite, and austenite of the super duplex is clearly observed in the hardness and modulus nanoindentation map. In the middle, a region with low hardness and modulus correlates with an EBSD performed before the nanoindentation map. The interactions of the electrons with the sample during the EBSD may have affected the mechanical properties of the surface of the sample.

Statistical analysis using the GMM clustering algorithm is performed on this sample as three phases are present on this material: sigma, austenite, and ferrite [10]. In Figure 34, comparison between the X and Y position contour and cluster plots is exhibited. In Figure 35, a histogram representation of the clustered data is illustrated for both hardness and elastic modulus. The “Experimental data” includes all the data, while “Ferrite”, “Austenite”, “Sigma” and “Noise cluster” represent the data labeled on each cluster, and in Figure 36 the cluster plot is presented.

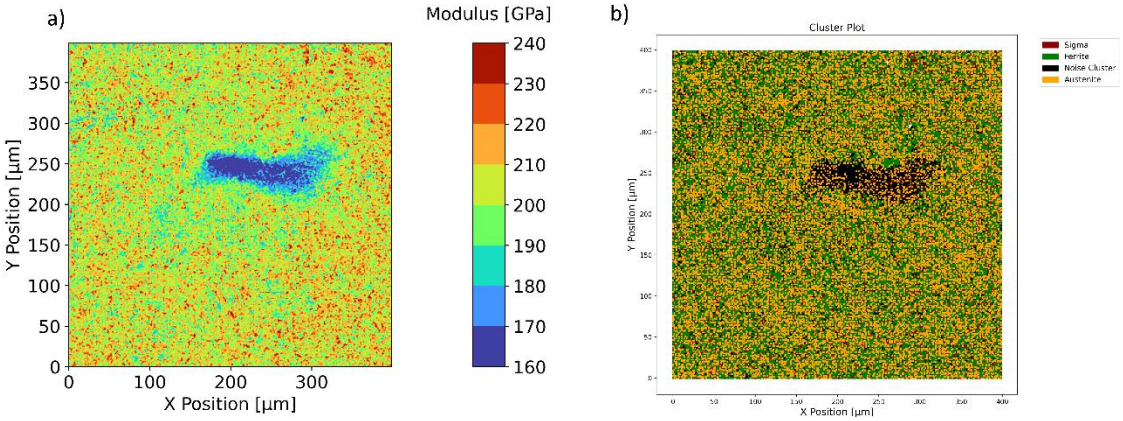

Figure 34: comparison between a) X position vs Y position contour plot and b) X position vs Y position cluster plot for the SD sample. Source: author image.

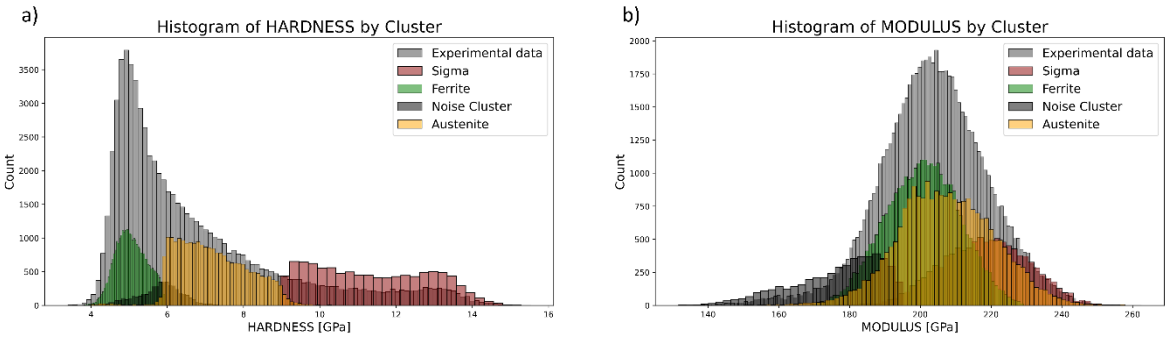

Figure 35: contribution of each cluster of a) hardness and b) elastic modulus for the 316L region of the SD sample. Source: author image.

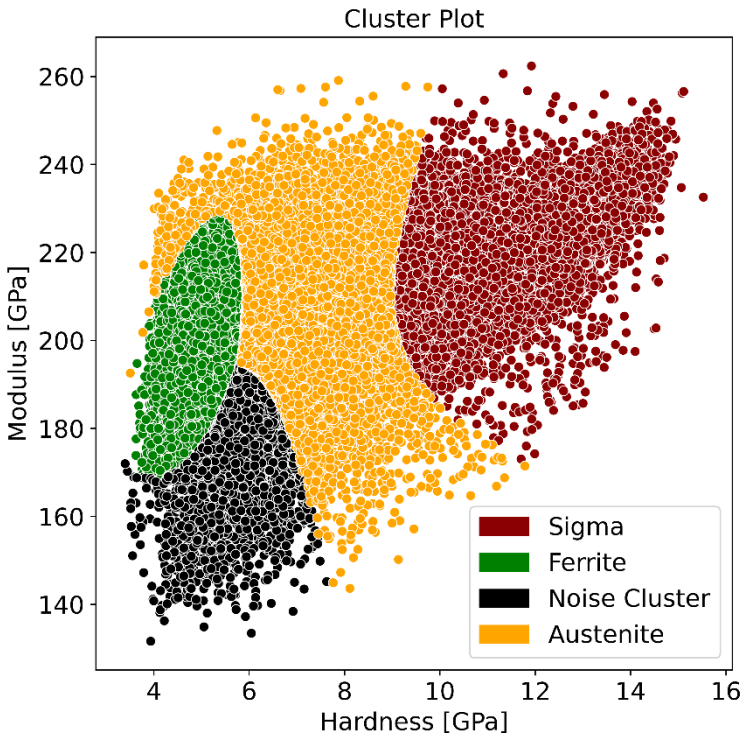

Figure 36: hardness in function of modulus representation of the phases identified by the clustering algorithm for the SD sample. Source: author image.

With the Figure 34 comparison is possible to visualize the quality of the phase identification made by the clustering algorithm, that seems to be acceptable as both images can be correlated. It should be noted that the elastic modulus contour plot was chosen because the region affected by the previous EBSD test is not visible on the hardness contour plot.

If the experimental data is plotted as the elastic modulus in function of the hardness, as Figure 36, information about the data dispersion is obtained. The green cluster is the one with lower grade of dispersion, indicating that is the one that fits better with the Gaussians distribution. The remaining detected phases have a considerable level of dispersion, indicating that care must be taken as maybe

the clusters are not discerned correctly – there are uncertainty on the resulting clusters -. For this reason, it cannot be assumed that the phase identification has been done perfectly. Future work must be done regarding this topic.

On Figure 37, the hardness (a) and EBSD (b) images are overlapped with the SEM – showing the microstructure of the sample –. The correlation of both analysis fits with the SEM image of the microstructure.

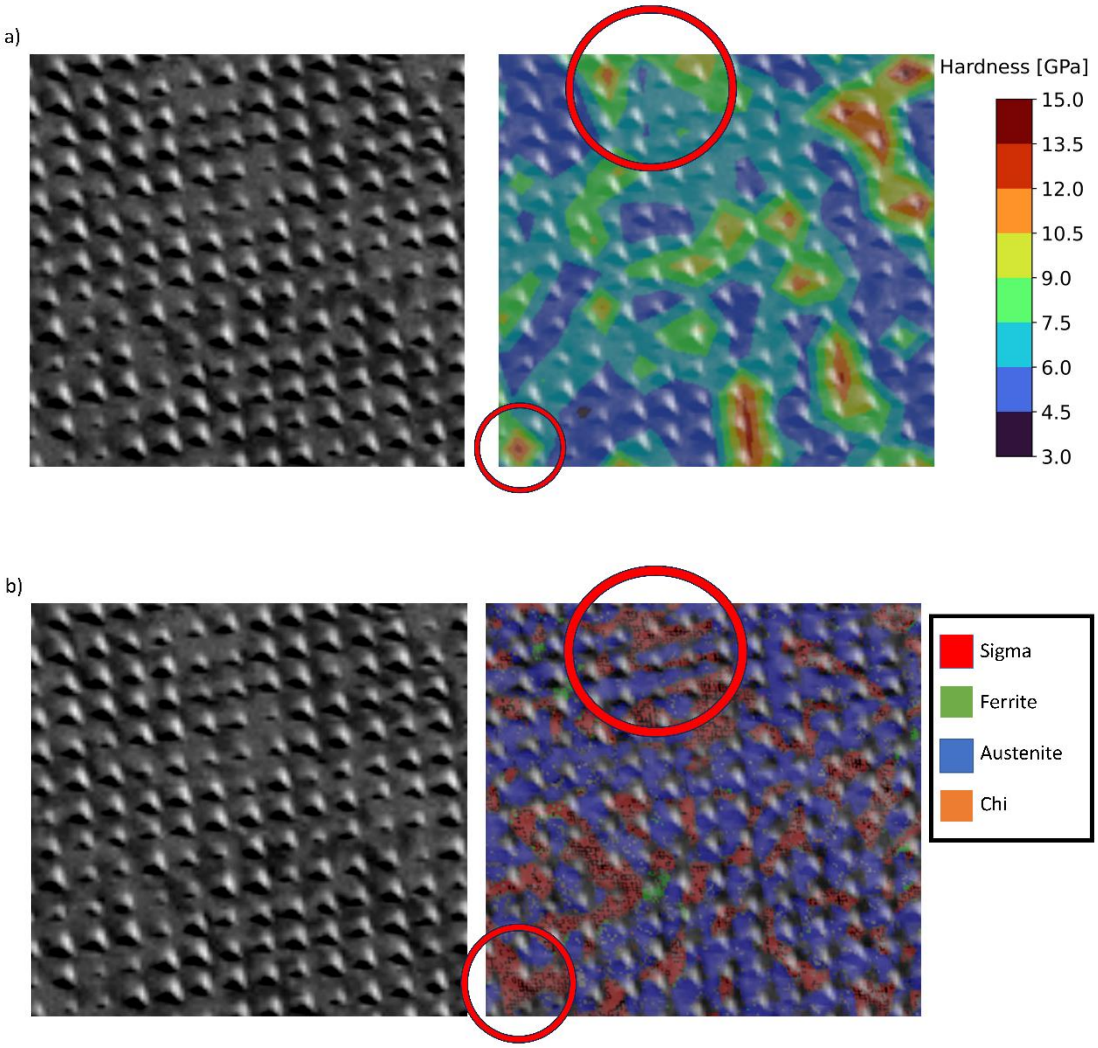

Figure 37: correlation between a) SEM and hardness contour plot, and b) SEM and EBSD image. RAW SEM image is included for better understanding. Source: author image.

By analyzing both correlations it is demonstrated that the Sigma phase is the hardest one. Looking at the regions marked with red circles, it can be observed that the presence of sigma phase increases the hardness values, reaching 10-13 GPa, approximately. Moreover, the areas where ferrite or austenite phases are present, the hardness values become lower – between 3 and 7.5 GPa -.

5.2.3. Addition of BN to a 316L steel sample

The study of the two remaining samples have been focused on the microstructural effects that adding boron carbides (BN) implies. For this reason, a 316L steel sample – which acts as a reference – have been tested and compared with another containing a mixture of 316L and BN.

5.2.3.1. 316L reference sample

In Figure 38, the contour plots of the 316L steel sample are presented. As have been seen previously on section 5.1.1, austenite elongated grains with different crystallographic orientations are visible.

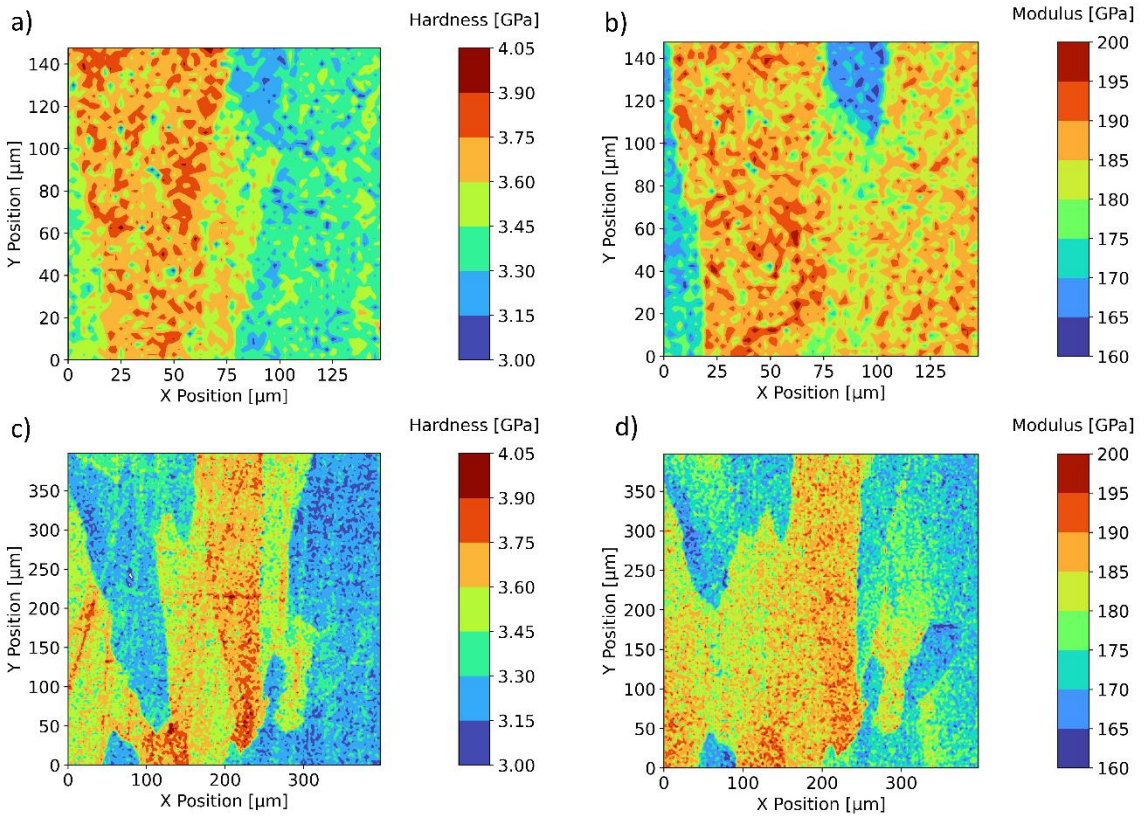

Figure 38: Contour plots of the 316L reference sample. a) and b) maps have 150x150 µm dimensions, whether c) and d) have 400x400 µm dimensions. Source: author image.

Analyzing the Figure 38 c) and d) contour plots of the 316L steel reference sample, the results are the same as the ones obtained on the 316L+V4E with transition structure – this is the reason why statistical analysis are not performed -. Two clearly different crystallographic orientations can be identified that fits with the large and columnar grains, corresponding to the austenite phase.

5.2.3.2. 316L+BN

In Figure 39, the contour plots of the big part of the 316L + BN sample are presented.

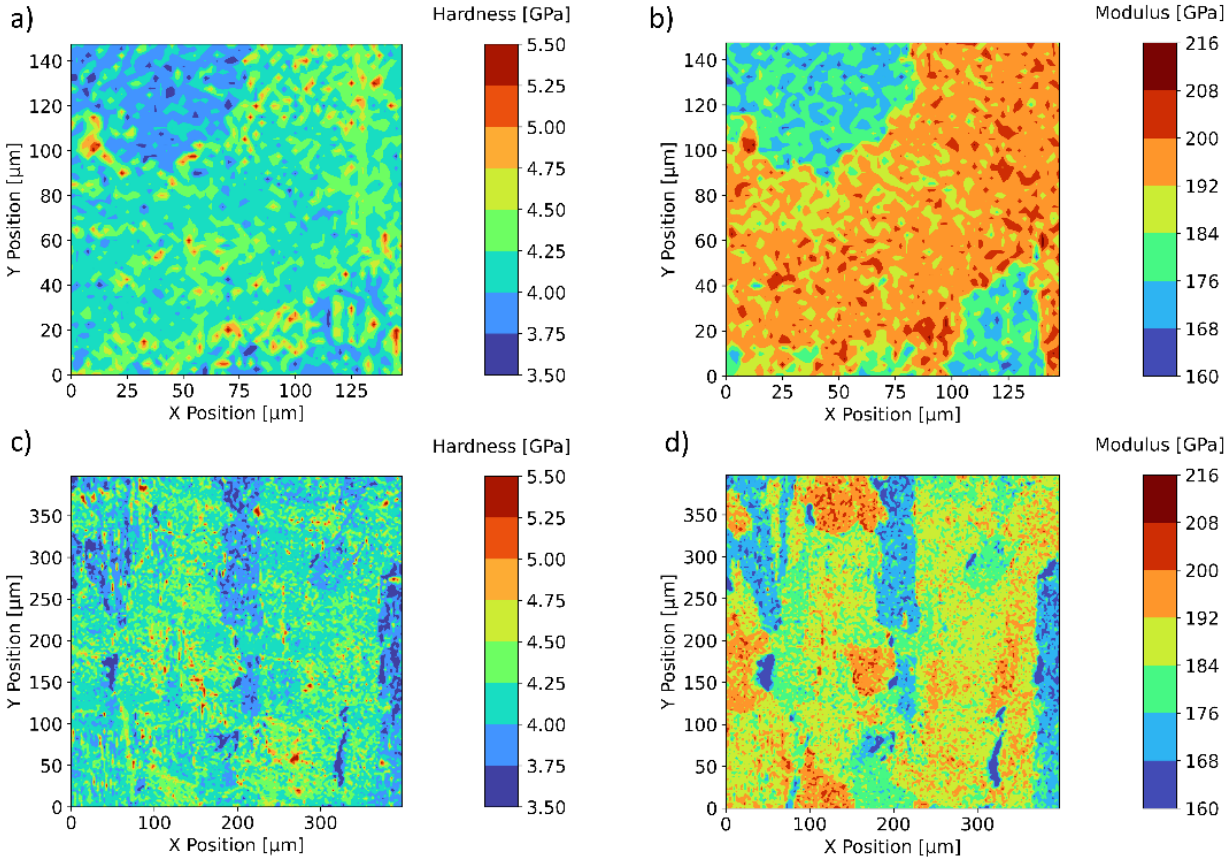

Figure 39: Contour plots of the big part of the 316L+BN sample. a) and b) maps have 150x150 µm dimensions, whether c) and d) have 400x400 µm dimensions. Source: author image.

An elongated texture can be seen constituted by the different crystallographic orientations found on the 316L reference sample. Furthermore, small hard regions – visible in a) and c) contour plots – corresponding to the boron carbides can be spotted.

The effect of the boron carbides seems to consist of grain refinement, especially if Figures 38 d) and 39 d) are compared. This should involve an improvement of the mechanical properties, but it is not in this case as neither hardness nor elastic modulus have been improved considerably.

Figure 40 shows the same information as Figure 39, but for the small part of the sample.

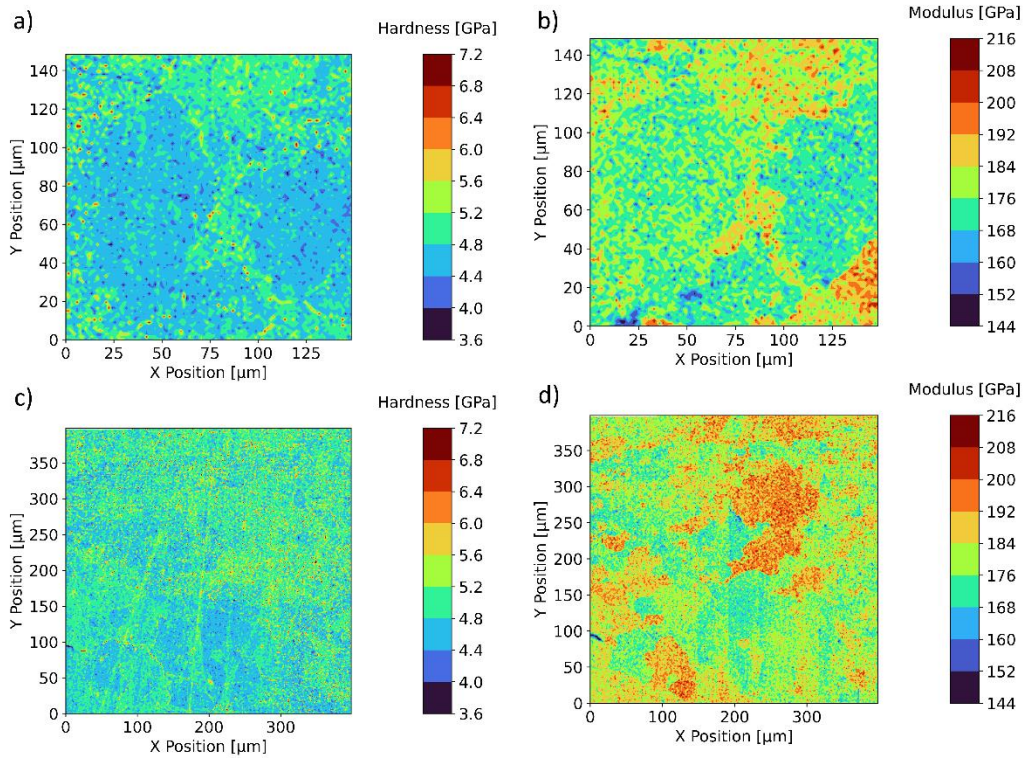

Figure 40: Contour plots of the small part of the 316L+BN sample. a) and b) maps have 150x150 µm dimensions, whether c) and d) have 400x400 µm dimensions. Source: author image.

Slightly different results were obtained but, in general terms, the conclusions are the same. Different crystallographic orientations of the 316L austenitic phase that fits with its grains can be identified. Although, this time the grains are less elongated and even smaller -this makes sense, as the big part of the sample was cut by the Z manufacturing plane, while the small part was cut by the XY one -. Also, it should be noted that the number of boron carbides detected on the hardness contour plots have become considerably lower, although on the modulus contour plots seems to be clearly detected on the same way. Two possible explanations for this are: (i) the small-size and low density of the BN powder makes difficult to process the powder blend, and it is possible that part of the powder is expelled away from the melt pool during processing and (ii) it is possible that part of the BN that is incorporated in the melt gets dissolved in the 316L matrix. In future studies it would be interesting to further analyze the presence of Boron and Nitrogen in the 316L by using techniques such as EDS.

In Figures 41 to 43, the statistical analysis for the big part of the sample is performed. In Figure 41 the comparison between the cluster and the contour plots is presented, showing an acceptable correlation. In Figure 42, the contribution of each cluster is plotted, and in Figure 43 the hardness in function of modulus cluster plot is exposed.

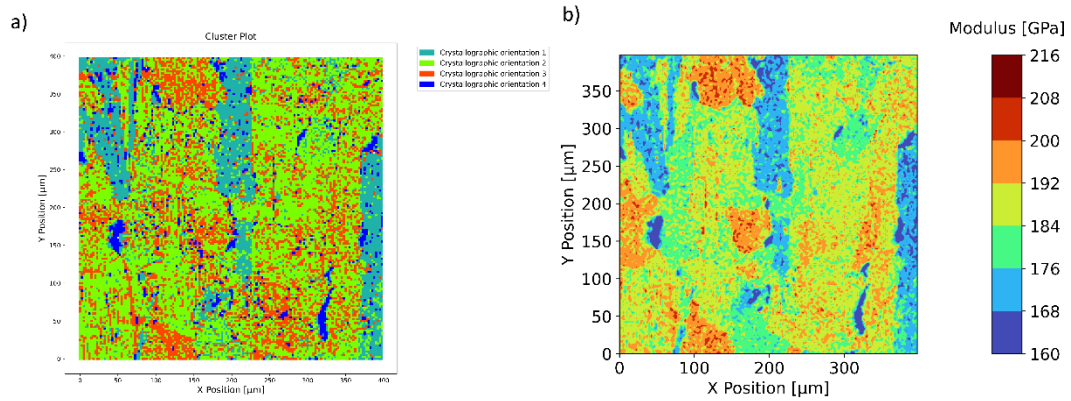

Figure 41: comparison between a) X position vs Y position contour plot and b) X position vs Y position cluster of the big part of the 316L+BN sample. Source: author image.

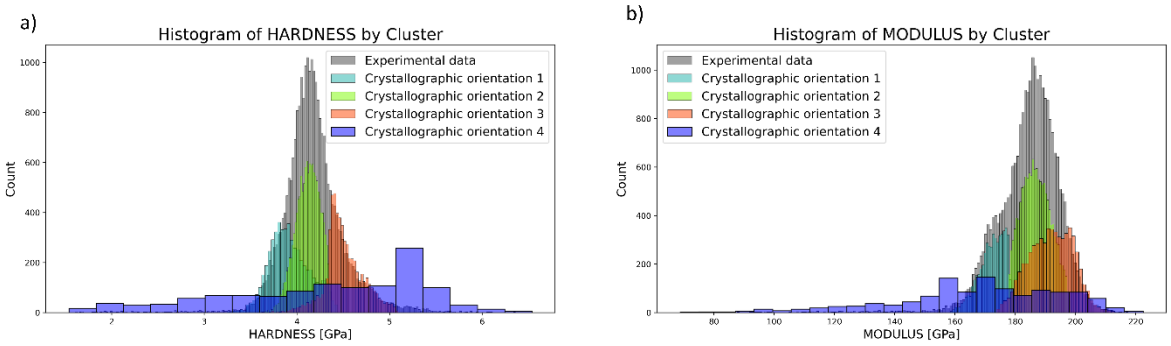

Figure 42: contribution of each cluster of a) hardness and b) elastic modulus of the big part of the 316L+BN sample . Source: author image.

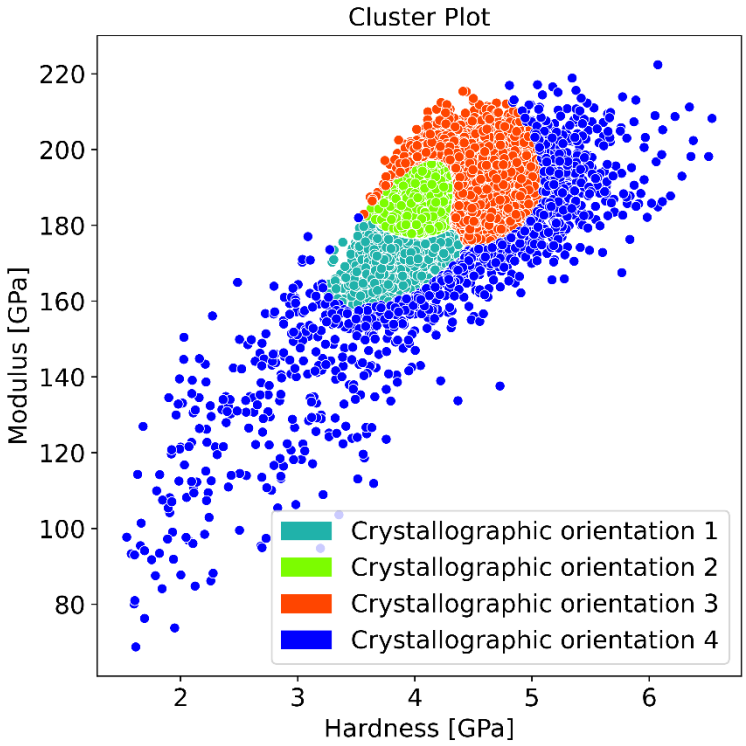

Figure 43: hardness in function of modulus representation of the phases identified by the clustering algorithm of the big part of the 316L+BN sample. Source: author image.

It must be noted that, in this case, the algorithm seems to work acceptably fine as the cluster and contour plots have a great similarity. Nevertheless, taking a closer look at the comparison, some points of the crystallographic orientation 1 cluster are labeled as the crystallographic orientation 3 cluster, and vice versa. This makes sense, as the contribution of crystallographic orientations 1 to 3 clusters overlap each other although it seems that fits correctly to the experimental data, see Figure 42. This is verified on the hardness in function of modulus cluster plot, where the dispersion of the data corresponding to those clusters does not have a considerable dispersion. Regarding the crystallographic orientation 4, the high-level dispersion of its data and the fact that does not fit in the contribution of each cluster representation means that can be considered as “Noise data” – data that cannot be classified in the other clusters -.

In Figures 44 to 46, the same information is presented as Figures 41 to 43, but for the small part of the sample.

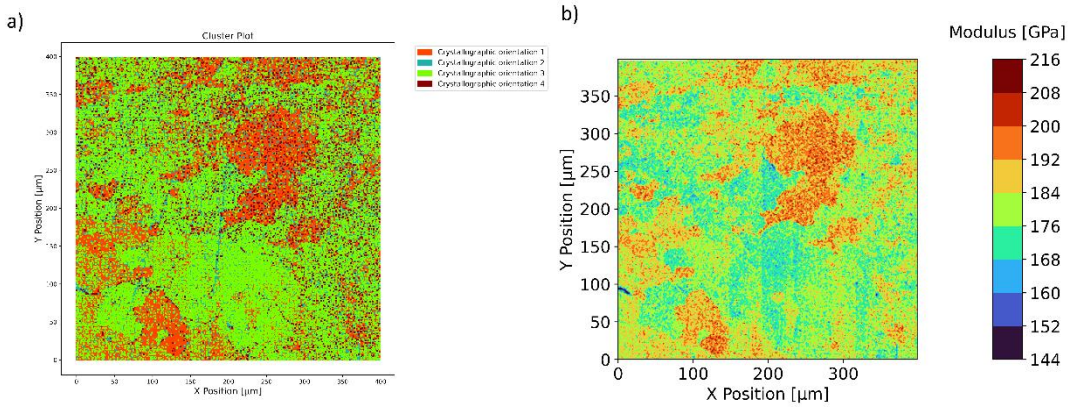

Figure 44: comparison between a) X position vs Y position contour plot and b) X position vs Y position cluster plot of the small part of the 316L+BN sample. Source: author image.

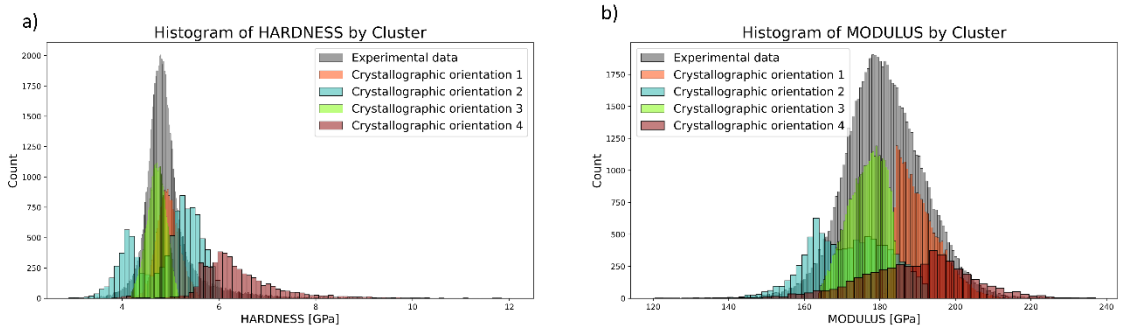

Figure 45: contribution of each cluster of a) hardness and b) elastic modulus for the small part of the 316L+BN sample . Source: author image.

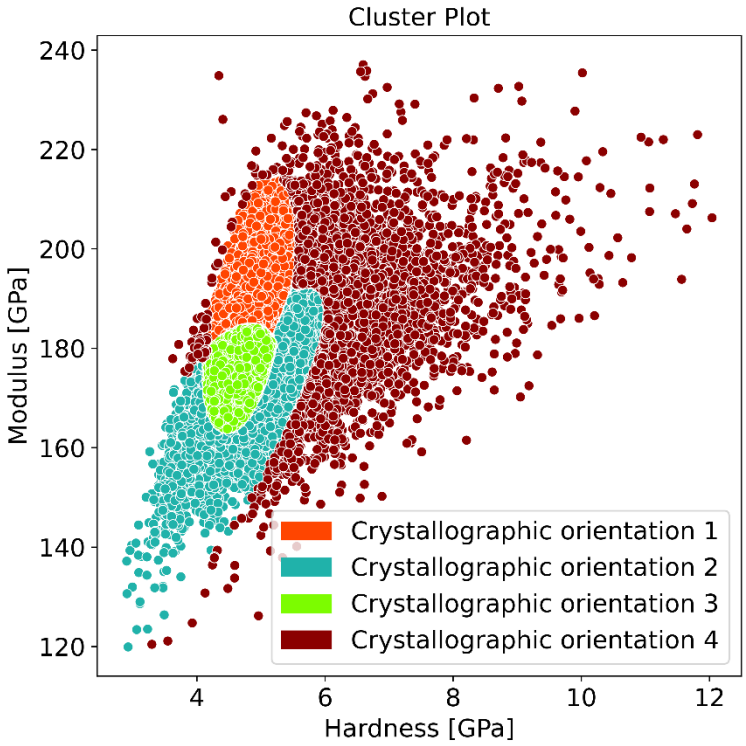

Figure 46: hardness in function of modulus representation of the phases identified by the clustering algorithm of the small part of the 316L+BN sample. Source: author image.

In this case, it seems that the algorithm worked acceptably fine as well as for the big part, considering that the cluster and contour plots are similar each other. The crystallographic orientation 1 seems to be the best identified cluster, while there is uncertainty regarding the remaining ones. The crystallographic 2 and 3 clusters are confused with each other clearly, see Figure 44. Taking a closer look to the contribution of each cluster – Figure 45 -, it can be confirmed that the crystallographic orientation 2 cluster is not identified correctly, as it does not fit to the experimental data. Regarding the crystallographic orientation 4 cluster, the dispersion of data showed in the hardness in function of modulus cluster plot indicates that possibly it may be a "noise cluster". Nevertheless, it seems that its contribution fits – almost – to the experimental data and, analyzing comparison made in Figure 44, it can be observed that this cluster corresponds to the data points with higher elastic modulus value.

6. Additional considerations

On this chapter, additional discussions and considerations arisen from the realization of this study are exposed and explained.

6.1. Selecting the most effective statistical method

As it has been mentioned previously on chapter 2.2, there are multiple clustering algorithms to perform statistical analysis of the nanoindentation data, and each one has its advantages and drawbacks. One of the main challenges of this study was to select the algorithm that better works for the phase identification of the materials. To achieve this, all the clustering algorithms were applied to multiple samples and the one that showed better results was chosen as the best one.

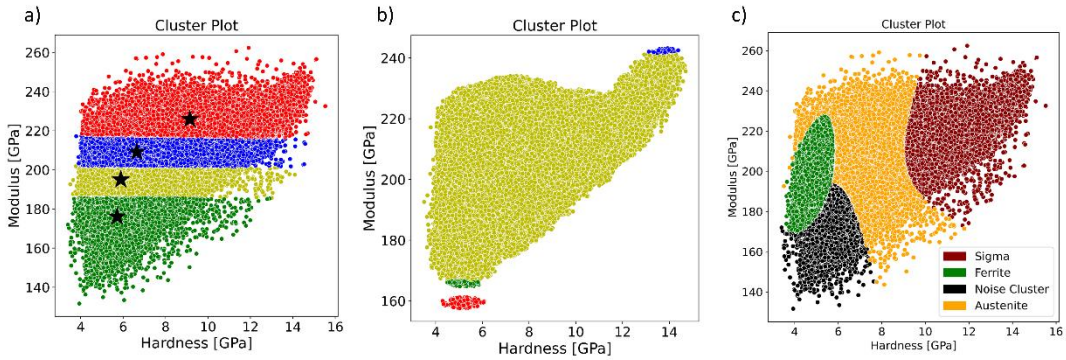

Figure 47: comparison between the modulus in function of hardness cluster plots of a) K-means b) DBSCAN and c) GMM clustering algorithms applied to the SD sample. Source: author image

The first tried algorithm was K-means. As it is shown in Figure 47 a), the classification of the data was effectuated horizontally, which makes no sense. The black stars markers indicate the centroids of each cluster as it is a needed parameter to the algorithm.

DBSCAN algorithm group the data in three small clusters and in another big one. Apparently, it seems that this is a strange classification, but it is not enough to consider the algorithm as invalid. But looking at the Y position in function of X position contour plot – represented in Figure 48 -, DBSCAN can be discarded.

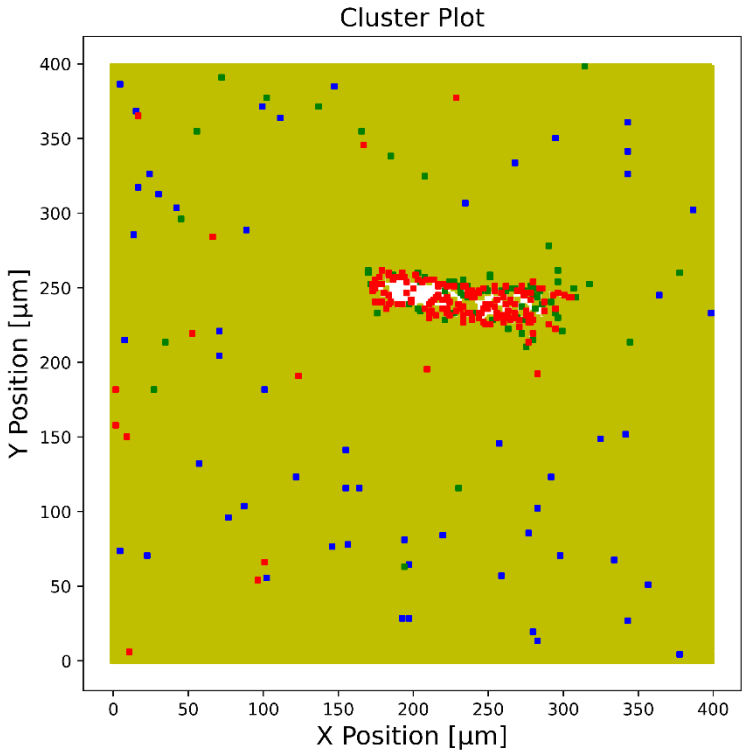

Figure 48: Y position in function of X position cluster plot of the SD sample, made using DBSCAN algorithm. Source: author image.

Regarding the HAC algorithm, it cannot be applied to this data because the resources needed were too high and the computation time was too long. Therefore, HAC was discarded.

Considering all the information presented, GMM algorithm was chosen the best one as the classification of the data seems to be the one that gives the best results.

6.2. The main problem of the GMM method

Although the GMM clustering algorithm was chosen as the best one – discarding K-means, HAC and DBSCAN -, it does not work perfectly to perform the phase identification as in most cases the Gaussian distributions that the algorithm fits to the experimental data overlap each other, involving the misestimation of the phase in some regions of the nanoindentation map performed previously.

An example of this could be observed on the histograms of the SD sample (Figure 35): there are a considerable quantity of area that corresponds to two or more Gaussian distribution and, therefore, two or more phases. Another example is shown in Figure 49, in which the same phenomenon occurs.

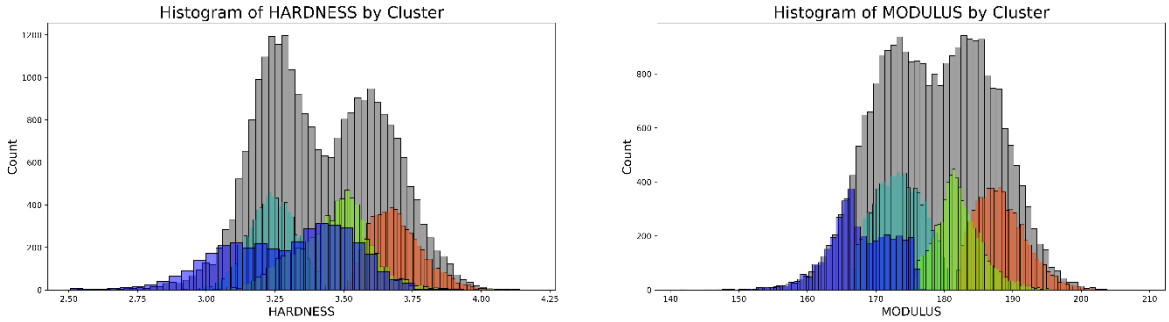

Figure 49: hardness and modulus data histograms of the 316L reference sample with the Gaussian distributions overlapped. Source: author image.

It must be said that, for this example – 316L reference sample -, the distributions correspond to crystallographic orientations instead of phases. Nevertheless, this does not affect to the reasoning.

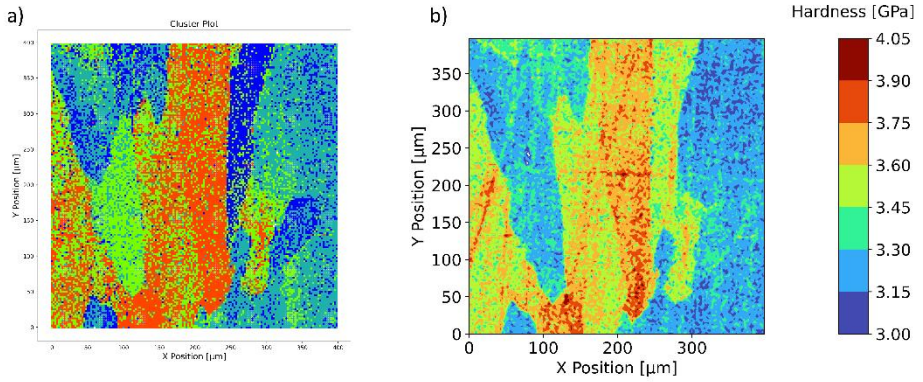

Figure 50: comparison between a) cluster plot and b) contour plot of the 316L reference sample. Source: author image.

On Figure 50 a misestimation of the crystallographic orientations can be spotted, as the blue region on the 250 µm X position of the cluster plot does not match with its corresponding area on the contour plot.

6.3. Affectations in the nanoindenter measures

When analyzing the contour plots made from the nanoindentation map data, there are multiple aspects to consider. The presence of defects on the surface of the sample is one of the most common ones. If the area to be indented have defects such as scratches, pores, or dirt, they will affect both the hardness and elastic modulus measures of the specific area containing these defects. An example of this can be found in Figure 22 c).

Another affectation that can appear to the results – and therefore ruining it – is the tip wear. This phenomenon takes place when a high number of indentations are made without calibrating the tip.

In Figure 22 d), an example of this could be seen. When performing the nanoindentation map, the modulus values – which are most sensitive than the hardness ones – gradually increase, masking the real values.

7. Expectations for the future

As is has been exposed during this study, the statistical analysis of the samples – the 316L+V4X transition, gradient and Super Duplex – has been negatively affected by the main problem of the inaccuracy that the GMM clustering algorithm – and generally the unsupervised algorithm methods - involves. By the application of these statistical methodologies, it has been observed that, when the phases or crystallographic orientations are close each other, the clustering algorithm is not able to set exactly where the border between clusters is. For this reason and as a result of this study, further investigation to improve the clusters delimitation of the applied algorithm – GMM – is proposed. Alternatively, it is proposed to carry out an in-depth study to find another possible clustering algorithms – with its necessary parameters, if needed – that can fit the data coming from nanoindentation tests. By realizing this, a robust and automated method to do the phase identification could be achieved.

Conclusions

At the end of this investigation, the initial proposed objectives have been successfully accomplished: First, the nanoindentation basic theory has been understood. This has been a fundamental requirement to develop all the investigation. Nanoindentation tests were performed successfully to a group of AM samples – made by PBF-EB – and the results were treated and plotted to analyze the mechanical properties and perform microstructural characterization. At the same time, research of different statistical methods has been done to select which one would give us the best results. Finally, a correlation between the contour plots with the microstructure obtained through characterization techniques – EBSD, EDS and SEM – has been performed successfully.

Apart from achieving the initial objectives, multiple conclusions have been reached.

- High-speed nanoindentation is a fast method to obtain mechanical properties at micro-length scale of large areas.
- Microstructure and different crystallographic orientations can be observed using high-speed nanoindentation. This is especially important as, in some cases, it would be an alternative of another characterization techniques such as EBSD, SEM or EDS.
- Although the Gaussian Mixture Model can identify the phases in some samples, in others such as 316L+V4E the model does not work well. In general, unsupervised models have demonstrated that are not able to fit well the identified phases. Therefore, there are still some advances to do in statistical analysis.
- The gradient of layers of 316L and V4E show that the mix of the two materials can successfully improve the hardness values. This could be a competitive advantage as modifying the mechanical properties of complex shape parts using AM would be possible.
- Sometimes it is better to compare with modulus contour plot and, in other cases, with the hardness contour plot. It is suspected that this is because of the crystallographic orientations

Economic analysis

In this section all the cost of the study is specified. Only the equipment has involved costs as the samples has been sent by Carlos Botero.

Table 3: detailed pricing of the used equipment [81].

Equipment	Time of use [h]	Cost [€/h]	Total cost [€]
iMicro nanoindenter	550	20	11000
Optical microscope	5	9	45
SEM	3	187.5	562.5
Desktop SEM	10	45	450

Table 4: detailed pricing of the required services [82].

Equipment	Number of samples	Cost [€/sample]	Total cost [€]
EBSD	4	300	1200

It must be noted that the EBSD analysis was performed on only one sample, but four attempts were needed.

Table 5: total price of the use of equipment.

Equipment	Price [€]
iMicro nanoindenter	11000
Optical microscope	45
SEM	562.5
Desktop SEM	450
EBSD	1200
TOTAL	13257.5

Bibliography

[1] H. J. Böhm, “Micromechanics,” *Encyclopedia of Continuum Mechanics*, pp. 1621–1628, 2020, doi: 10.1007/978-3-662-55771-6_10/COVER.

[2] G. V. Jagadeesh and S. Gangi Setti, “A review on micromechanical methods for evaluation of mechanical behavior of particulate reinforced metal matrix composites,” *Journal of Materials Science*, vol. 55, no. 23. Springer, pp. 9848–9882, Aug. 01, 2020. doi: 10.1007/s10853-020-04715-2.

[3] P. Sudharshan Phani and W. C. Oliver, “A critical assessment of the effect of indentation spacing on the measurement of hardness and modulus using instrumented indentation testing,” *Mater Des*, vol. 164, Feb. 2019, doi: 10.1016/j.matdes.2018.107563.

[4] S. Gordon *et al.*, “Micromechanical mapping of polycrystalline cubic boron nitride composites by means of high-speed nanoindentation: Assessment of microstructural assemblage effects,” *J Eur Ceram Soc*, 2022, doi: 10.1016/j.jeurceramsoc.2022.08.047.

[5] C. Fraley and A. E. Raftery, “How Many Clusters? Which Clustering Method? Answers Via Model-Based Cluster Analysis.” [Online]. Available: http://comjnl.oxfordjournals.org/

[6] A. Koptyug *et al.*, “Compositionally-tailored steel-based materials manufactured by electron beam melting using blended pre-alloyed powders,” *Materials Science and Engineering A*, vol. 771, Jan. 2020, doi: 10.1016/j.msea.2019.138587.

[7] S. Roos and L. E. Rännar, “Process window for electron beam melting of 316ln stainless steel,” *Metals (Basel)*, vol. 11, no. 1, pp. 1–11, Jan. 2021, doi: 10.3390/met11010137.

[8] L. E. Rännar, A. Koptyug, J. Olsén, K. Saeidi, and Z. Shen, “Hierarchical structures of stainless steel 316L manufactured by Electron Beam Melting,” *Addit Manuf*, vol. 17, pp. 106–112, Oct. 2017, doi: 10.1016/j.addma.2017.07.003.

[9] Y. Zhong *et al.*, “Additive manufacturing of 316L stainless steel by electron beam melting for nuclear fusion applications,” *Journal of Nuclear Materials*, vol. 486, pp. 234–245, Apr. 2017, doi: 10.1016/j.jnucmat.2016.12.042.

[10] S. Roos, C. Botero, and L. E. Rännar, “Electron beam powder bed fusion processing of 2507 super duplex stainless steel. as-built phase composition and microstructural

properties," *Journal of Materials Research and Technology*, vol. 24, pp. 6473–6483, May 2023, doi: 10.1016/j.jmrt.2023.04.230.

[11] C. Botero et al, "Additive Manufacturing of a Cold-Work Tool Steel using Electron Beam Melting".

[12] C. A. Botero *et al.*, "Microstructural and mechanical evaluation of a cr-mo-v cold-work tool steel produced via electron beam melting (Ebm)," *Materials*, vol. 14, no. 11, Jun. 2021, doi: 10.3390/ma14112963.

[13] A. Koptyug *et al.*, "Compositionally-tailored steel-based materials manufactured by electron beam melting using blended pre-alloyed powders," *Materials Science and Engineering A*, vol. 771, Jan. 2020, doi: 10.1016/j.msea.2019.138587.

[14] M. B. C. A. B. V. V. P. and E. C. A. Koptyug, "Developing new materials for electron beam melting: Experiences and challenges".

[15] A. Koptyug, C. Botero, W. Sjöström, M. Bäckström, L.-E. Rännar, and A. S. Tremsin, "Electron Beam Melting: from Shape Freedom to Material Properties Control at Macro- and Microscale."

[16] F. Johansson, "Functionally gradient lamellas produced with Electron Beam Melting A method for additive manufacturing of multi-material components using dissimilar metal powders within one process."

[17] J. M. Sanchez, A. Pascual, I. Vicario, J. Albizuri, T. Guraya, and H. Galarraga, "Microstructure and Phase Formation of Novel Al80Mg5Sn5Zn5X5 Light-Weight Complex Concentrated Aluminum Alloys," *Metals 2021, Vol. 11, Page 1944*, vol. 11, no. 12, p. 1944, Dec. 2021, doi: 10.3390/MET11121944.

[18] R. Pederson, "Microstructure and Phase Transformation of Ti-6Al-4V," 2002.

[19] H. Clemens, S. Mayer, and C. Scheu, "Microstructure and Properties of Engineering Materials," *Neutrons and Synchrotron Radiation in Engineering Materials Science: From Fundamentals to Applications: Second Edition*, pp. 1–20, Jan. 2017, doi: 10.1002/9783527684489.CH1.

[20] M. Chegini, M. H. Shaeri, R. Taghiabadi, S. Chegini, and F. Djavanroodi, "The Correlation of Microstructure and Mechanical Properties of In-Situ Al-Mg2Si Cast Composite Processed by Equal Channel Angular Pressing," *Materials*, vol. 12, no. 9, 2019, doi: 10.3390/MA12091553.

[21] W. C. Oliver and G. M. Pharr, “Measurement of hardness and elastic modulus by instrumented indentation: Advances in understanding and refinements to methodology,” 2004. [Online]. Available: www.mrs.org/publications/jmr/policy.html

[22] B. Vignesh, W. C. Oliver, G. S. Kumar, and P. S. Phani, “Critical assessment of high speed nanoindentation mapping technique and data deconvolution on thermal barrier coatings,” *Mater Des*, vol. 181, Nov. 2019, doi: 10.1016/j.matdes.2019.108084.

[23] J. J. Roa *et al.*, “Intrinsic hardness of constitutive phases in WC-Co composites: Nanoindentation testing, statistical analysis, WC crystal orientation effects and flow stress for the constrained metallic binder,” *J Eur Ceram Soc*, vol. 35, no. 13, pp. 3419–3425, Nov. 2015, doi: 10.1016/j.jeurceramsoc.2015.04.021.

[24] J. J. Roa *et al.*, “Hall-Petch strengthening of the constrained metallic binder in WC–Co cemented carbides: Experimental assessment by means of massive nanoindentation and statistical analysis,” *Materials Science and Engineering A*, vol. 676, pp. 487–491, Oct. 2016, doi: 10.1016/j.msea.2016.09.020.

[25] M. Sau *et al.*, “High-Throughput Nanoindentation Mapping of Additively Manufactured T91 Steel,” *JOM*, 2022, doi: 10.1007/s11837-022-05189-0.

[26] “Dependence of nanoindentation hardness ... grains in metastable stainless steels”.

[27] X. Chen, D. Hou, Y. Han, X. Ding, and P. Hua, “Clustering analysis of grid nanoindentation data for cementitious materials,” *J Mater Sci*, vol. 56, no. 21, pp. 12238–12255, Jul. 2021, doi: 10.1007/s10853-021-05848-8.

[28] F. Bernachy-Barbe, “A data analysis procedure for phase identification in nanoindentation results of cementitious materials,” *Materials and Structures/Materiaux et Constructions*, vol. 52, no. 5, Oct. 2019, doi: 10.1617/s11527-019-1397-y.

[29] J. M. Wheeler, D. E. J. Armstrong, W. Heinz, and R. Schwaiger, “High temperature nanoindentation: The state of the art and future challenges,” *Curr Opin Solid State Mater Sci*, vol. 19, no. 6, pp. 354–366, Dec. 2015, doi: 10.1016/J.COSSMS.2015.02.002.

[30] “High Temperature Nanoindentation - The State-of-the-art Laser Heating Technique - Keysight Technical Backgrounder.” https://about.keysight.com/en/newsroom/backgrounders/G200/ (accessed May 30, 2023).

[31] E. D. Hintsala, U. Hangen, and D. D. Stauffer, "High-Throughput Nanoindentation for Statistical and Spatial Property Determination," *JOM*, vol. 70, no. 4, pp. 494–503, Apr. 2018, doi: 10.1007/S11837-018-2752-0/FIGURES/8.

[32] C. M. Magazzeni *et al.*, "Nanoindentation in multi-modal map combinations: a correlative approach to local mechanical property assessment," *J Mater Res*, vol. 36, 123AD, doi: 10.1557/s43578-020-00035-y.

[33] A. Orozco-Caballero, C. Gutierrez, B. Gan, and J. M. Molina-Aldareguia, "High-throughput nanoindentation mapping of cast IN718 nickel-based superalloys: influence of the Nb concentration," *J Mater Res*, vol. 36, 123AD, doi: 10.1557/s43578-021-00133-5.

[34] J. M. Wheeler, "Mechanical phase mapping of the Taza meteorite using correlated high-speed nanoindentation and EDX," *J Mater Res*, doi: 10.1557/s43578-020-00056-7.

[35] H. Besharatloo and J. M. Wheeler, "Influence of indentation size and spacing on statistical phase analysis via high-speed nanoindentation mapping of metal alloys," *J Mater Res*, vol. 36, no. 11, pp. 2198–2212, Jun. 2021, doi: 10.1557/s43578-021-00214-5.

[36] G. Constantinides and F.-J. Ulm, "The nanogranular nature of C-S-H," *J Mech Phys Solids*, vol. 55, pp. 64–90, 2007, doi: 10.1016/j.jmps.2006.06.003.

[37] M. Sau *et al.*, "High-Throughput Nanoindentation Mapping of Additively Manufactured T91 Steel," *JOM*, 2022, doi: 10.1007/S11837-022-05189-0.

[38] X. Chen, D. Hou, Y. Han, X. Ding, and P. Hua, "Clustering analysis of grid nanoindentation data for cementitious materials," *J Mater Sci*, vol. 56, no. 21, pp. 12238–12255, Jul. 2021, doi: 10.1007/S10853-021-05848-8.

[39] G. Konstantopoulos, E. P. Koumoulos, and C. A. Charitidis, "Testing novel portland cement formulations with carbon nanotubes and intrinsic properties revelation: Nanoindentation analysis with machine learning on microstructure identification," *Nanomaterials*, vol. 10, no. 4, Apr. 2020, doi: 10.3390/nano10040645.

[40] F. E. Bock, R. C. Aydin, C. J. Cyron, N. Huber, S. R. Kalidindi, and B. Klusemann, "A review of the application of machine learning and data mining approaches in continuum materials mechanics," *Front Mater*, vol. 6, p. 110, Apr. 2019, doi: 10.3389/FMATS.2019.00110/BIBTEX.

[41] A. R. Durmaz *et al.*, "A deep learning approach for complex microstructure inference," *Nature Communications 2021 12:1*, vol. 12, no. 1, pp. 1–15, Nov. 2021, doi: 10.1038/s41467-021-26565-5.

[42] Z. Zhang, J. Qin, Z. Ma, X. Pang, and Y. Zhou, "Comparison of three different deconvolution methods for analyzing nanoindentation test data of hydrated cement paste," *Cem Concr Compos*, vol. 138, p. 104990, 2023, doi: 10.1016/j.cemconcomp.2023.104990.

[43] A. Dhal, R. S. Haridas, P. Agrawal, S. Gupta, and R. S. Mishra, "Mapping hierarchical and heterogeneous micromechanics of a transformative high entropy alloy by nanoindentation and machine learning augmented clustering", doi: 10.1016/j.matdes.2023.111957.

[44] S. Gautham and S. Sasmal, "Journal Pre-proof Constitutive relations of nanoscale hydration products present in engineered cementitious composites from machine learning assisted experimental nanoindentation," *Journal of Building Engineering*, 2023, doi: 10.1016/j.jobe.2023.106912.

[45] Y. Li *et al.*, "Big data nanoindentation characterization of cross-scale mechanical properties of oilwell cement-elastomer composites," 2022, doi: 10.1016/j.conbuildmat.2022.129190.

[46] M. Lesufi, S. O. Akinwamide, W. Makoana, L. Tshabalala, and P. A. Olubambi, "Nanoindentation and Corrosion Behaviour of 410 Stainless Steel Fabricated Via Additive Manufacturing," *Transactions of the Indian Institute of Metals*, Mar. 2022, doi: 10.1007/S12666-022-02736-W.

[47] A. Reiser *et al.*, "Metals by Micro-Scale Additive Manufacturing: Comparison of Microstructure and Mechanical Properties 1910491 (2 of 20)," *Adv. Funct. Mater*, vol. 2020, p. 1910491, 2020, doi: 10.1002/adfm.201910491.

[48] J. England *et al.*, "Nanoindentation Hardness and Corrosion Studies of Additively Manufactured 316L Stainless Steel," *J Mater Eng Perform*, vol. 31, no. 8, pp. 6795–6805, Aug. 2022, doi: 10.1007/S11665-022-06703-W.

[49] A. J. Birnbaum, H. Ryou, J. C. Steuben, A. P. Iliopoulos, K. J. Wahl, and J. G. Michopoulos, "Nested size effects in the nanoindentation response of additively manufactured 316L stainless steel," 2020, doi: 10.1016/j.matlet.2020.128570.

[50] E. Jiménez-Piqué, "Indentation of ceramics," in *Encyclopedia of Materials: Technical Ceramics and Glasses*, Elsevier, 2021, pp. 718–732. doi: 10.1016/B978-0-12-818542-1.00089-8.

[51] Y. Chang, M. Lin, U. Hangen, S. Richter, C. Haase, and W. Bleck, "Revealing the relation between microstructural heterogeneities and local mechanical properties of complex-phase steel by correlative electron microscopy and nanoindentation characterization," *Mater Des*, vol. 203, May 2021, doi: 10.1016/j.matdes.2021.109620.

[52] K. Y. X. M. Designed Research; X, "Exploring the origins of the indentation size effect at submicron scales," vol. 118, no. 23, p. 2021, 2021, doi: 10.1073/pnas.2025657118/-/DCSupplemental.

[53] G. M. Pharr, E. G. Herbert, and Y. Gao, "The indentation size effect: A critical examination of experimental observations and mechanistic interpretations," *Annu Rev Mater Res*, vol. 40, pp. 271–292, 2010, doi: 10.1146/annurev-matsci-070909-104456.

[54] X. Ma, W. Higgins, Z. Liang, D. Zhao, G. M. Pharr, and K. Y. Xie, "Exploring the origins of the indentation size effect at submicron scales," *Proc Natl Acad Sci U S A*, vol. 118, no. 30, Jul. 2021, doi: 10.1073/PNAS.2025657118.

[55] O. Petruš *et al.*, "Indentation size effect in the hardness measurements of high entropy carbides," *Ceram Int*, Nov. 2022, doi: 10.1016/J.CERAMINT.2022.11.185.

[56] H. Besharatloo *et al.*, "Novel mechanical characterization of austenite and ferrite phases within duplex stainless steel," *Metals (Basel)*, vol. 10, no. 10, pp. 1–15, Oct. 2020, doi: 10.3390/met10101352.

[57] "10 Machine Learning Algorithms to Know in 2023 | Coursera." https://www.coursera.org/articles/machine-learning-algorithms (accessed May 31, 2023).

[58] "What Is Unsupervised Machine Learning? | DataRobot." https://www.datarobot.com/wiki/unsupervised-machine-learning/ (accessed Apr. 13, 2023).

[59] "Unsupervised Machine learning - Javatpoint." https://www.javatpoint.com/unsupervised-machine-learning (accessed Apr. 13, 2023).

[60] “Gaussian Mixture Modelling (GMM). Making Sense of Text Data using… | by Daniel Foley | Towards Data Science.” https://towardsdatascience.com/gaussian-mixture-modelling-gmm-833c88587c7f (accessed Jun. 12, 2023).

[61] “The 5 Clustering Algorithms Data Scientists Need to Know | by George Seif | Towards Data Science.” https://towardsdatascience.com/the-5-clustering-algorithms-data-scientists-need-to-know-a36d136ef68 (accessed Apr. 13, 2023).

[62] “Clustering Algorithms - K-means Algorithm.” https://www.tutorialspoint.com/machine_learning_with_python/clustering_algorithms_k_means_algorithm.htm (accessed Apr. 13, 2023).

[63] “When to use K-means clustering - Crunching the Data.” https://crunchingthedata.com/when-to-use-k-means-clustering/ (accessed Apr. 13, 2023).

[64] “How the Hierarchical Clustering Algorithm Works - Dataaspirant.” https://dataaspirant.com/hierarchical-clustering-algorithm/#t-1608531820435 (accessed Jun. 01, 2023).

[65] “Hierarchical Clustering – LearnDataSci.” https://www.learndatasci.com/glossary/hierarchical-clustering/ (accessed Jun. 01, 2023).

[66] “DBSCAN Clustering Algorithm in Machine Learning - KDnuggets.” https://www.kdnuggets.com/2020/04/dbscan-clustering-algorithm-machine-learning.html (accessed Jun. 01, 2023).

[67] “DBSCAN Clustering — Explained. Detailed theorotical explanation and… | by Soner Yıldırım | Towards Data Science.” https://towardsdatascience.com/dbscan-clustering-explained-97556a2ad556 (accessed Jun. 01, 2023).

[68] “How Density-based Clustering works—ArcGIS Pro | Documentation.” https://pro.arcgis.com/en/pro-app/latest/tool-reference/spatial-statistics/how-density-based-clustering-works.htm (accessed Jun. 01, 2023).

[69] M. Mahmudur Rahman Khan, M. Abu Bakr Siddique, R. Bente Arif, and M. Rahman Oishe, “ADBSCAN: Adaptive Density-Based Spatial Clustering of Applications with Noise for Identifying Clusters with Varying Densities”.

[70] "An Introduction to EBSD." https://www.azom.com/article.aspx?ArticleID=11770 (accessed Apr. 12, 2023).

[71] "Kikuchi lines." https://www.doitpoms.ac.uk/tlplib/diffraction-patterns/kikuchi.php (accessed Jun. 01, 2023).

[72] "Scanning Electron Microscopy (SEM)." https://serc.carleton.edu/research_education/geochemsheets/techniques/SEM.html (accessed Jun. 07, 2023).

[73] "Scanning Electron Microscopy - Nanoscience Instruments." https://www.nanoscience.com/techniques/scanning-electron-microscopy/ (accessed Jun. 07, 2023).

[74] A. F. Ismail, K. C. Khulbe, and T. Matsuura, "RO Membrane Characterization," *Reverse Osmosis*, pp. 57–90, Jan. 2019, doi: 10.1016/B978-0-12-811468-1.00003-7.

[75] "Energy-dispersive detector (EDS)." https://serc.carleton.edu/msu_nanotech/methods/eds.html (accessed Jun. 01, 2023).

[76] "Energy Dispersive Analysis — Metallurgical Engineering Services." https://www.metengr.com/testing-services/chemical-analysis/energy-dispersive-x-ray-eds (accessed Jun. 01, 2023).

[77] "Introduction to Energy Dispersive X-ray Spectrometry (EDS)."

[78] "Energy-Dispersive X-ray Spectroscopy (EDS) - Chemistry LibreTexts." https://chem.libretexts.org/Courses/Franklin_and_Marshall_College/Introduction_to_Materials_Characterization__CHM_412_Collaborative_Text/Spectroscopy/Energy-Dispersive_X-ray_Spectroscopy_(EDS) (accessed Jun. 01, 2023).

[79] "Ceramic Powders Non-Oxide Powders-Black and White."

[80] A. Biserova Tahchieva, N. Llorca-Isern, and J. M. Cabrera, "Duplex and Superduplex Stainless Steels: 2 microstructure and properties evolution by surface modificaction processes 4."

[81] "Price list — Barcelona Research Center in Multiscale Science and Engineering — UPC. Universitat Politècnica de Catalunya." https://multiscale.upc.edu/en/infrastructure/services-and-prices (accessed Jun. 09, 2023).

[82] “https://serveiscientificotecnics.upc.edu/ca/cerca/tarifes-externes-sct-upc-versio-web.pdf.”

Annex

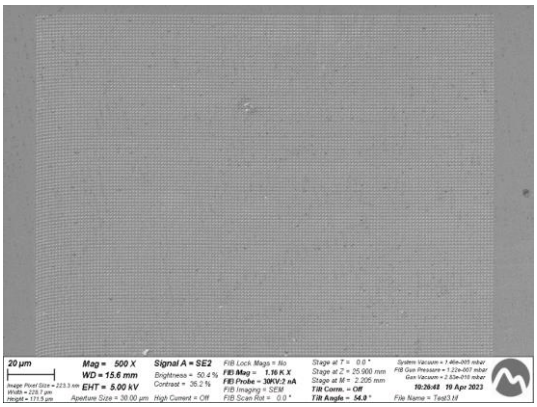
20 µm
Mag = 500 X
WD = 15.6 mm
EHT = 5.00 kV
Signal A = SE2

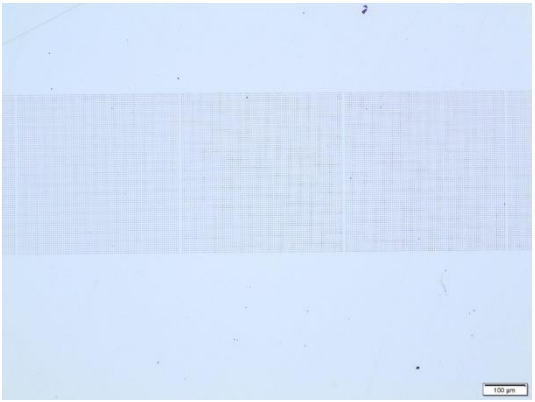

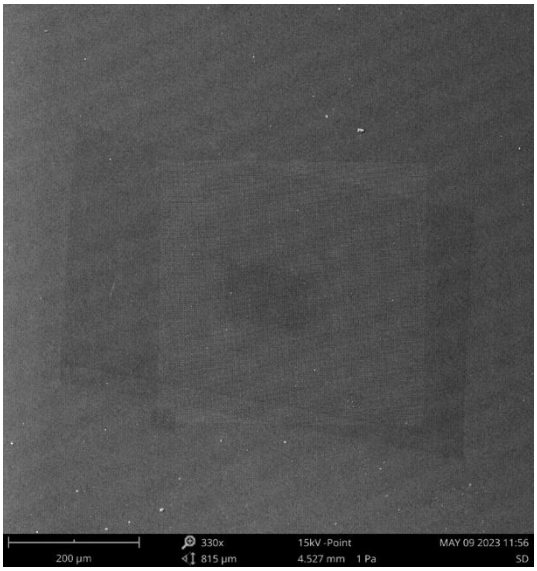
200 µm
330x
815 µm
15kV -Point
4.527 mm 1 Pa
MAY 09 2023 11:56
SD

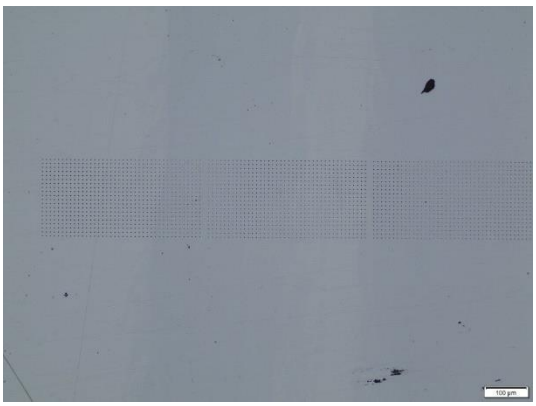

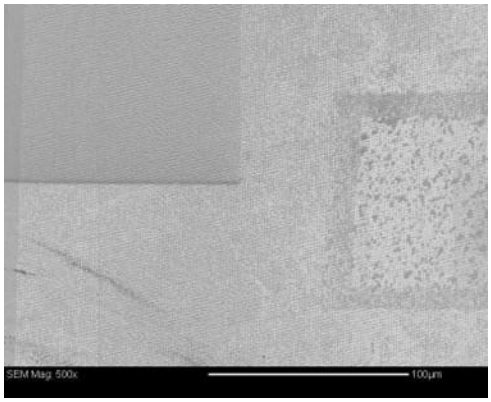
SEM Mag: 500x
100µm

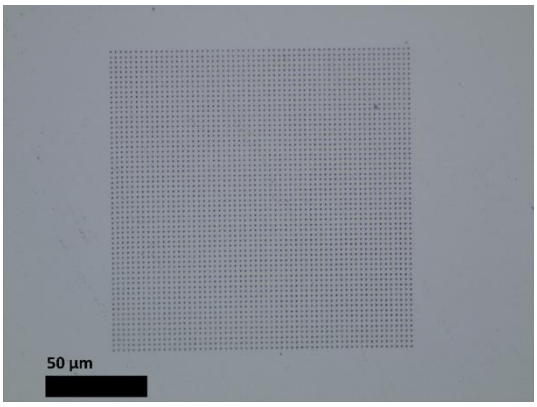
50 µm

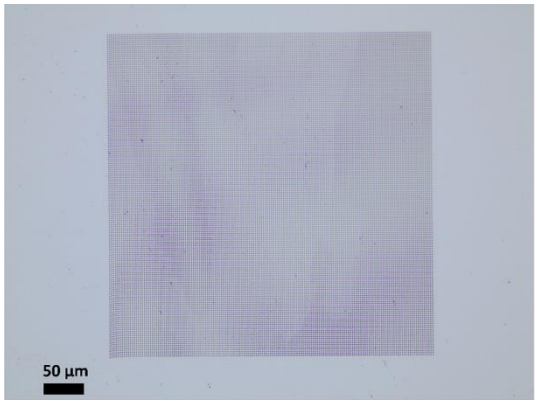
50 µm

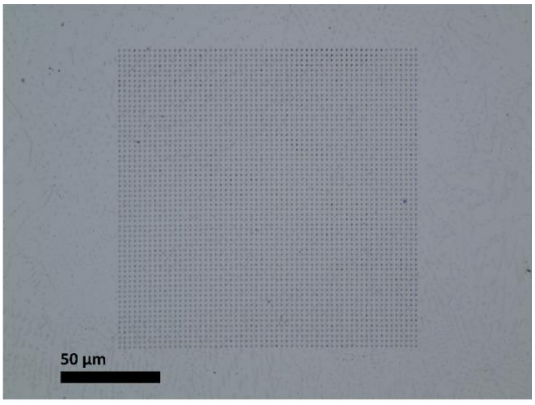
50 µm

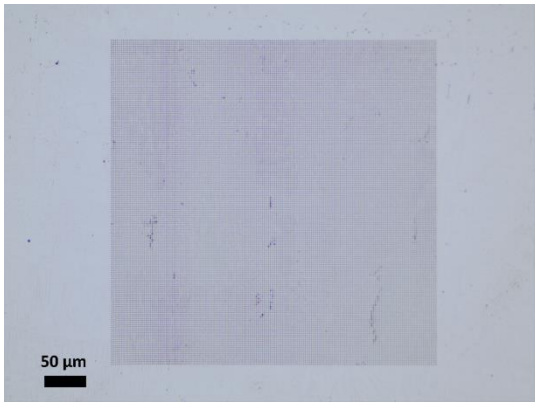
50 µm

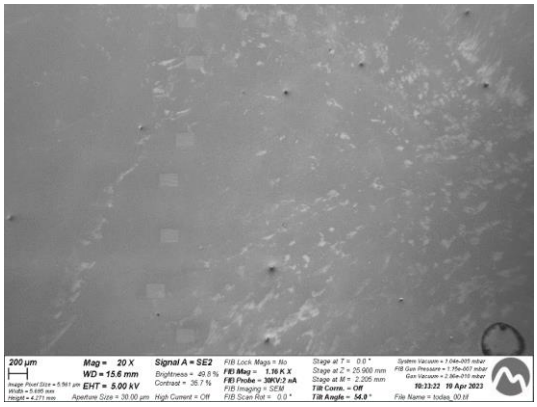
200 µm
Mag = 20 X
WD = 15.6 mm
EHT = 5.00 kV
Signal A = SE2
FIB Mag = 1.16 K X
FIB Probe = 30KV;2 nA
Tilt Corrn. = Off
Tilt Angle = 54.0 °
16:33:23 19 Apr 2013